A Hybrid Method to Estimate Specific Differential Phase and Rainfall With Linear Programming and Physics Constraints

Hao Huang, Guifu Zhang, *Senior Member, IEEE*, Kun Zhao, and Scott E. Giangrande

***Abstract*—A hybrid method of combining linear programming (LP) and physical constraints is developed to estimate specific differential phase ($K_{\rm DP}$) and to improve rain estimation. The hybrid $K_{\rm DP}$ estimator and the existing estimators of LP, least squares fitting, and a self-consistent relation of polarimetric radar variables are evaluated and compared using simulated data. Simulation results indicate the new estimator's superiority, particularly in regions where backscattering phase ($\delta_{\rm hv}$) dominates. Furthermore, a quantitative comparison between auto-weather-station rain-gauge observations and $K_{\rm DP}$-based radar rain estimates for a Meiyu event also demonstrate the superiority of the hybrid $K_{\rm DP}$ estimator over existing methods.**

***Index Terms*—Radar application, radar data processing.**

I. Introduction

In RECENT years, the dual-polarization upgrade of weather radar networks has yielded new measurements and information that provide valuable new insights into cloud and precipitation processes over conventional weather radar observations. In addition to the radar reflectivity factor (Z_H), polarimetric radars measure several new quantities, including the differential reflectivity factor ($Z_{\rm DR}$), specific differential phase ($K_{\rm DP}$), and copolar cross-correlation coefficient ($\rho_{\rm hv}$) [1]. These polarimetric measurements, when used alone or in combination, help to significantly improve hydrological applications, including quantitative precipitation estimation (QPE) [2], [3]. In particular, the inclusion of $K_{\rm DP}$, defined as the range derivative of the differential propagation phase ($\phi_{\rm DP}$) between the two polarized signals, offers many advantages for QPE, particularly in challenging heavier rainfall contexts [4]. Specifically, $K_{\rm DP}$ is better correlated with the rain rate R at all weather radar frequencies and is immune to radar miscalibration, attenuation in precipitation, and partial beam blocking. Furthermore, $K_{\rm DP}$ has been successfully applied within bulk hydrometeor classification routines since it is uniquely sensitive to improve the designation of graupel and dendritic snow crystals [5].

Despite these known advantages for QPE, there are still issues in obtaining accurate $K_{\rm DP}$ estimates from the polarimetric radar measured differential phase ($\Phi_{\rm DP}$). Typically, $K_{\rm DP}$ is estimated from the range derivative of the measured ($\Phi_{\rm DP}$). However, the measured differential phase $\Phi_{\rm DP}$ is composed of the differential propagation phase ($\phi_{\rm DP}$), differential backscattering phase ($\delta_{\rm hv}$), and measurement errors including statistical/sampling error, ground clutters, side lobes, second-trip echoes, mixed-phase hydrometeors (large melting aggregates and hailstones), nonuniform beam filling, and so on [6]–[8]. This may be expressed as $\Phi_{\rm DP} = \phi_{\rm DP} + \delta_{\rm hv} + \varepsilon$ if ignoring certain error contributions from ground clutter, sidelobes, nonuniform beam filling, etc. Contributions from these terms can be mostly removed in the quality control procedure. To reduce effects of statistical errors ε, it is useful to smooth $\Phi_{\rm DP}$ so that the range derivative of $\phi_{\rm DP}$ can be correctly calculated. Nevertheless, excessive smoothing of $\Phi_{\rm DP}$ results in overly processed $K_{\rm DP}$ estimates that lose fine-scale precipitation features. For shorter wavelength radars and applications (e.g., X-band and C-band, with wavelengths of 3 and 5 cm, respectively), the $\delta_{\rm hv}$ may also contribute large errors to $K_{\rm DP}$ estimation [4]. Therefore, it is increasingly critical at shorter wavelengths to separate $\phi_{\rm DP}$ contributions from $\Phi_{\rm DP}$ accurately to reduce the error in $\phi_{\rm DP}$ for $K_{\rm DP}$ estimation, while keeping the inherent spatial structure of precipitation.

Many algorithms have been proposed toward obtaining accurate $K_{\rm DP}$ estimates from $\Phi_{\rm DP}$. One common method is to apply various forms of signal filters, such as FIR filter [9], [10] or wavelet analysis [11]. In these approaches, high-frequency components along the $\Phi_{\rm DP}$ radial measurement profiles are removed. The most basic approach has been to fit noisier $\Phi_{\rm DP}$ radial profiles with a smoothed one based on a median filter, a moving average, or more sophisticated averaging methods. Recently, an algorithm based on a Kalman filter approach was also proposed, suggesting improved estimation accuracy under lower signal-to-noise ratio (SNR) conditions [12].

Manuscript received March 7, 2016; revised July 5, 2016; accepted July 17, 2016. Date of publication October 19, 2016; date of current version November 29, 2016. This work was supported in part by the National Fundamental Research 973 Program of China under Grant 2013CB430101; by the National Natural Science Foundation of China under Grant 41475015, Grant 41275031 and Grant 41322032; and by the Program for New Century Excellent Talents in University of China. The work of S. E. Giangrande was supported by the U.S. Department of Energy under Contract No. DE-AC02-98CH10886. *(Corresponding authors: Kun Zhao and Guifu Zhang.)*

H. Huang and K. Zhao are with the Key Laboratory of Mesoscale Severe Weather of the Ministry of Education, School of Atmospheric Sciences, Nanjing University, Nanjing 210023, China (e-mail: zhaokun@nju.edu.cn).

G. Zhang is with the Key Laboratory of Mesoscale Severe Weather of the Ministry of Education, School of Atmospheric Sciences, Nanjing University, Nanjing 210023, China, and also with the School of Meteorology, University of Oklahoma, Norman, OK 73072 USA (e-mail: guzhang1@ou.edu).

S. E. Giangrande is with the Department of Environmental and Climate Sciences, Brookhaven National Laboratory, Upton, NY 11973 USA.

Color versions of one or more of the figures in this paper are available online at http://ieeexplore.ieee.org.

Digital Object Identifier 10.1109/TGRS.2016.2596295

Since $\delta_{\rm hv}$ contributions are typically less significant at the longer wavelengths in rain media (e.g., S-band, 10-cm wavelength), the operational dual-polarization WSR-88D network is able to implement a simple least squares fitting (LSF) method. For these radars, $K_{\rm DP}$ is estimated by applying LSF on multiple gates of $\Phi_{\rm DP}$ measurements over adaptive radial ranges. These filter lengths vary from approximately 2 to 6 km, based on the intensity of radar echo (Z_H), centered on that range gate [13]. This approach selects $\Phi_{\rm DP}$ data filtered over a relatively large radial range (6 km) for the moderate-to-weak echo ($Z_H < 40$ dBZ), and over a relatively small radial range (2 km) for strong echo ($Z_H > 40$ dBZ). The advantage of this adaptive range, or 'synthetic' solution, is that it is simple to implement operationally. The approach reflects a compromise that prevents $K_{\rm DP}$ from being overly smoothed in severe convective regions, while facilitating rainfall rate estimation by heavily smoothing within light precipitation regions where $K_{\rm DP}$ estimates are typically noisier.

Due to the fact that the sampling volume averaged axis ratio (ratio of minor axis and major axis) of raindrops is never larger than 1 [2], [14], intrinsic $K_{\rm DP}$ is nonnegative when the radar beam goes through liquid hydrometers. Nevertheless, the aforementioned estimation methods will occasionally produce negative $K_{\rm DP}$ estimates in rain due to contributions from the backscattering phase $\delta_{\rm hv}$, nonuniform beam filling, or other statistical errors of $\Phi_{\rm DP}$ measurements [15]. As $K_{\rm DP}$ estimates should be unbiased by $\delta_{\rm hv}$ at the longer wavelengths, Ryzhkov and Zrnic proposed to incorporate negative rainfall rate values into spatiotemporal integrals, such as using a formula $R = 40.6|K_{\rm DP}|^{0.866}{\rm sign}(K_{\rm DP})$ [8]. Similarly, to designate or better account for the role of negative $K_{\rm DP}$ values on hydrological applications including those originating from backscattering phase or other contributions, it is useful to examine statistical $K_{\rm DP} - Z_H$ relationships and replace physically unrealistic negative $K_{\rm DP}$ estimates with physically realistic values estimated from Z_H. Simply adopting the latter approach, $K_{\rm DP}$ and $K_{\rm DP}$-based rain-rate estimates may appear cosmetically more accurate, particularly at the rear or peripheral gradient regions of intense storms wherein negative $K_{\rm DP}$ regions are the most prominent. However, the ramifications for such substitutions are statistically important since artificial negative $K_{\rm DP}$ excursions are accompanied by artificial positive $K_{\rm DP}$ excursions. Therefore, the radial integral of $K_{\rm DP}$, which is related to $\phi_{\rm DP}$, would significantly increase due to the simple replacement of negative $K_{\rm DP}$, leading to an overestimation for the total accumulated rainfall (AR) from $K_{\rm DP}$-based rain-rate spatiotemporal integrals. Several methods including so-called "ZPHI" methods have been suggested to offset several of these concerns by constraining the substitutions according to the path-integrated differential phase [16].

Recently, an LP method [17] has been proposed that may mitigate the $\Phi_{\rm DP}$ noisiness and improve $K_{\rm DP}$ estimation simultaneously. The LP method is mainly based on linear optimization theory [18]. The basis for the method was to extract a $\phi_{\rm DP}$ curve that best minimizes the difference between this extracted curve and the measured $\Phi_{\rm DP}$ at a given series of linear constraints. For the initial proof-of-concept article, the assumption for nonnegative $K_{\rm DP}$ values served as an example constraint set [17]. Using simulated and real data sets, the approach indicated nonnegative $K_{\rm DP}$ estimates, monotonously increasing $\phi_{\rm DP}$, and unbiased AR estimation with better fine-tuned range distribution over conventional methods. Moreover, simplified self-consistency constraints such as $K_{\rm DP} = aZ_H^b$ were identified as possible means to further improve and constrain these methods but were not well developed in that study.

As highlighted by Giangrande *et al.* [17], Ryzhkov and Zrnic [8], and many others, relationships between $K_{\rm DP}$ and Z_H are commonly used to identify and adjust unreasonable $K_{\rm DP}$ values (or partial beam blockages in Z_H) since both measurements are related to rainfall intensity. However, $K_{\rm DP}$ and Z_H are approximately the 4.2nd and 6th moments of DSD, respectively [1], [4]; thus, their relationship is nonlinear, unstable, and easily affected by the variability of the raindrop size distributions (DSDs). Self-consistent (SC) relations, as proposed by Scarchilli [19], Vivekanandan [20], and Giangrande [21], have shown that Z_H, $Z_{\rm DR}$, and $K_{\rm DP}$ triplets reside within a limited and possibly exploitable 3-D space for rainfall studies, more stable than two-parameter $K_{\rm DP} - Z_H$ relations and are less affected by DSD variability. By using well-calibrated and attenuation-corrected Z_H and $Z_{\rm DR}$, it is possible to estimate $K_{\rm DP}$ from the self-consistency of polarimetric radar data (PRD). It can be expected that this estimation is always nonnegative and close to the intrinsic values. Unless highly contaminated by hail presence, the SC relations are useful information to be utilized in $K_{\rm DP}$ estimation.

Moreover, algorithms such as LSF, LP, and those benefitting from self-consistency have advantages and disadvantages. Therefore, this paper is motivated by an attempt to combine the best attributes of those methods into a more optimal approach for $K_{\rm DP}$ estimation. To make use of as much information provided by polarimetric measurements as possible, we propose a hybrid method that combines the strengths of LSF and SC under an enhanced LP framework to estimate $K_{\rm DP}$ in rain regions. This paper is organized as follows. Section II describes the methodology and implementation associated with the LSF, simplified LP, and basic SC approaches. Section III presents an ideal experiment and a comparison of the results from these algorithms. In Section IV, an enhanced LP hybrid method that better incorporates these three concepts is proposed and applied on the ideal case to show its advantages. Qualitative and quantitative comparisons of basic LSF, simple LP, and enhanced LP hybrid methods during a Meiyu event are present in Section V. Finally, a summary and some discussions on future work are given in Section VI.

II. Methodology

According to the textbook definition for $K_{\rm DP}$ [4], only $\Phi_{\rm DP}$ measurements from two range gates are needed to obtain the intrinsic value, as in $K_{\rm DP} = ((\phi_{\rm DP}(r_2) - \phi_{\rm DP}(r_1))/2(r_2 - r_1))$, provided that there are no errors in $\Phi_{\rm DP}$ measurements, i.e., $\Phi_{\rm DP}$ is identical to intrinsic $\phi_{\rm DP}$.

When errors exist in the measurements, this problem becomes ill-posed. Retrieving $K_{\rm DP}$ according to its definition would lead to an unpractical result, particularly when statistical errors of $\Phi_{\rm DP}$ are relatively large. Fortunately, in weather

$$\mathbf{M}_{n-(m-1)/2,n} = \begin{pmatrix} C_{S-G}(1) & \cdots & C_{S-G}(m) & 0_{m+1} & 0_{m+2} & \cdots & 0_n \\ 0_1 & C_{S-G}(1) & \cdots & C_{S-G}(m) & 0_{m+2} & \cdots & 0_n \\ & \cdots & & & & \cdots & \\ 0_1 & \cdots & 0_{n-m-1} & C_{S-G}(1) & \cdots & C_{S-G}(m) & 0_n \\ 0_1 & \cdots & 0_{n-m-1} & 0_{n-m} & C_{S-G}(1) & \cdots & C_{S-G}(m) \end{pmatrix} \quad (3)$$

systems and associated storm-scale research, precipitation regimes and DSD properties does not change significantly from gate to gate. Because of this, measurements of more than two gates are often used to determine the $K_{\rm DP}$. This estimation becomes overdetermined when multiple measurements are involved in evaluating one variable [22]. All the aforementioned methods concern the issue of solving this overdetermined system and obtaining outcomes close to the intrinsic values. The $K_{\rm DP}$ estimation methods of LSF, LP, and self-consistency are reviewed here.

A. LSF

LSF is a common regression approach to obtain approximate solutions for an over-determined system. When the $K_{\rm DP}$ of an intermediate range gate needs to be determined, multiple $\Phi_{\rm DP}$ measurements (with errors) from the gates adjacent along the radial construct the whole system. Generally, the number of gates to be included should be determined mainly according to the standard deviation of the errors, which depends on the SNR of the radar data, estimation error of $\Phi_{\rm DP}$, and the variability of $K_{\rm DP}$ along the radial. As employed by the WSR-88D radar and CSU-CHILL radar [23] systems, we apply piecewise LSF on adaptive lengths with respect to echo intensity, i.e., Z_H. Two sets of experiments with different adaptive lengths are run to examine the dependence of LSF on the filter lengths in the succeeding section. One experiment uses the same adaptive lengths as those used by WSR-88D, i.e., 2 km (6 km) for gates where Z_H is beyond (below) 40 dBZ. The other one uses twice the WSR-88D adaptive lengths. The LSF formula is applied on $\Phi_{\rm DP}$ measurements at the gates within the adaptive lengths to obtain the $K_{\rm DP}$ estimate at the intermediate gate, i.e.,

$$K_{\rm DP} = \frac{\sum_{i=1}^{n} \left\{ \left[\Phi_{\rm DP}(i) - \overline{\Phi}_{\rm DP} \right] \bullet \left[r(i) - \overline{r} \right] \right\}}{2 \sum_{i=1}^{n} \left[r(i) - \overline{r} \right]^2} \quad (1)$$

where the overbar "−" means an averaged value, and r is the distance of $\Phi_{\rm DP}$ measurements from the radar.

B. LP

As proposed by Giangrande *et al.* [17], results from the LP with nonnegative constraints are summarized as follows. The main idea is optimizing $\phi_{\rm DP}$ under the physical constraints of rain. We denote the n-gate raw differential phase ray with $\mathbf{b} = (b_1, b_2, \ldots, b_n)$ and the filtered or processed ray with $\mathbf{x} = (x_1, x_2, \ldots, x_n)$, respectively. The LP problem is set as minimizing the difference between $\mathbf{b}$ and $\mathbf{x}$, i.e., $f = \sum_{i=1}^{n} |x_i - b_i|$. To mathematically deal with the absolute value, an intermediate vector $\mathbf{z} = (z_1, z_2, \ldots, z_n)$ is introduced that represents the variables that appear in the cost function. Regardless of whether $x_i - b_i$ is positive, negative, or zero, $z_i \geq |x_i - b_i|$ is always equivalent to the combination of two inequalities $z_i \geq x_i - b_i$ and $z_i \geq b_i - x_i$. Now, the minimization of f becomes the minimization of the n-term cost function $\sum_{i=1}^{n} z_i$ under two sets of constraints: $z_i - x_i \geq -b_i$ and $z_i + x_i \geq b_i$. Mathematically, we let $\mathbf{x}_c = (\mathbf{z}, \mathbf{x})^T$ be the independent variable of the LP problem. Now, the cost function $\sum_{i=1}^{n} z_i$, i.e., sum of the elements of $\mathbf{z}$, can be rewritten as a dot product $\mathbf{c} \bullet \mathbf{x}_c$, with the coefficient vector expressed as $\mathbf{c} = (1_1, \ldots, 1_n, 0_{n+1}, \ldots, 0_{2n})$. It was noted by Giangrande *et al.* [17] that potential missing data in the observations can be handled by setting the weights of the corresponding gates to zeros.

The matrix–vector form of the LP problem becomes minimizing $\mathbf{c} \bullet \mathbf{x}_c$ under the constraint of $\mathbf{A}\mathbf{x}_c \geq \mathbf{b}$, in which $\mathbf{A} = \begin{pmatrix} \mathbf{I}_n & -\mathbf{I}_n \\ \mathbf{I}_n & \mathbf{I}_n \end{pmatrix}$, and $\mathbf{I}_n$ is the $n \times n$ identity matrix. If there are no other constraints, the cost function reduces to zero when $\mathbf{x}$ equals to $\mathbf{b}$. When we add a nonnegative $K_{\rm DP}$ constraint to the LP problem as in Giangrande *et al.* [17], a $(n - ((m-1)/2)) \times n$ matrix $\mathbf{M}_{n-(m-1)/2,n}$ is employed to convert the filtered differential phase to its derivative, $K_{\rm DP}$. The matrix $\mathbf{M}_{n-(m-1)/2,n}$ is composed of coefficients of the m-point Savitzky–Golay $(S-G)$ second-order polynomial derivative filter, i.e.,

$$C_{S-G}(i) = \frac{6(2i - m - 1)}{m(m+1)(m-1)}, \quad i = 1, 2, \ldots, m \quad (2)$$

yielding (3), shown at the top of the page, where 0_j means zero at the jth column. With the m-point derivative filters involved, $K_{\rm DP}$ array can be expressed as $\mathbf{M}_{n-(m-1)/2,n}\mathbf{x}^T$. The linear inequality $\mathbf{M}_{n-(m-1)/2,n}\mathbf{x}^T \geq \mathbf{Z}_{n-(m-1)/2}$ serving as the nonnegative $K_{\rm DP}$ constraint can be merged into the now augmented parts of the matrix–vector form of the LP problem, in which $\mathbf{Z}_{n-(m-1)/2}$ is a zero vector. The modified algebraic form is now minimizing $\mathbf{c} \bullet \mathbf{x}_c$ under the constraint of $\mathbf{A}_{\rm AUG}\mathbf{x}_c \geq \mathbf{b}_{\rm AUG}$, which is the combination of the minimization and nonnegative constraint. The augmented matrix $\mathbf{A}_{\rm AUG}$ and vector $\mathbf{b}_{\rm AUG}$ can be expressed as

$$\mathbf{A}_{\rm AUG} = \begin{pmatrix} \mathbf{I}_n & -\mathbf{I}_n \\ \mathbf{I}_n & \mathbf{I}_n \\ \mathbf{Z}_{n-(m-1)/2,n} & \mathbf{M}_{n-(m-1)/2,n} \end{pmatrix} \quad (4)$$

$$\mathbf{b}_{\rm AUG} = \left(-\mathbf{b}, \mathbf{b}, \mathbf{Z}_{n-(m-1)/2} \right)^T \quad (5)$$

respectively, where $\mathbf{Z}_{n-(m-1)/2,n}$ is a zero matrix. Many toolkits have been developed to solve LP problems [24], [25]. It is

noted that, SciPy [26] provides a very convenient way to obtain a satisfactory solution $\mathbf{x}_c$. $K_{\rm DP}$ estimates are obtained from the formula $\mathbf{K_{DP}} = \mathbf{M}_{n-(m-1)/2,n}\mathbf{x}^T$, in which $\mathbf{x}$ should be preprocessed with a smoothing filter.

It seems at first glance that the LP estimation system is a well-posed linear system when applied on the $K_{\rm DP}$ estimation problem because the numbers of measurements $(\Phi_{\rm DP})$ and state variables ($K_{\rm DP}$ or $\phi_{\rm DP}$ in this particular system) are the same. Yet, mathematically it will lead to a meaningless solution because of observation errors. However, the underlying principle is that, each m-point $S-G$ derivative filter in $\mathbf{M}_{n-(m-1)/2,n}\mathbf{x}^T$ connects $\phi_{\rm DP}$ of m gates with $K_{\rm DP}$ at the intermediate gate. This is an analogy to an LSF within each adaptive range. It is worth noting that adaptive derivative filters cannot be applied in the LP estimation method. These derivative filters act as a constraint of state variable $\phi_{\rm DP}$. If the lengths of the filters vary, $\phi_{\rm DP}$ would not be monotonous. This study does not further explore this problem. For the purpose of manifesting the effect of the $S-G$ derivative filter, the results from the LP method with derivative filters of 2- and 6-km lengths are shown.

C. Self-Consistency

Previous studies have shown that the intrinsic $K_{\rm DP}$ values are constrained well by the intrinsic Z_H and $Z_{\rm DR}$ [19]–[21]. Although the simple SC relation $K_{\rm DP} = aZ^b$ was identified as one possibility to set a threshold in the LP method [17], the usage of self-consistency was not thoroughly studied for $K_{\rm DP}$ or rainfall estimation, with emphasis on shorter wavelengths wherein such constraints are more beneficial [27]. To obtain the intrinsic SC relation, polarimetric radar variables should be calculated from *in situ* observations (DSD data in this case). The T-matrix method can be used to compute scattering amplitude of raindrops at different sizes [28], [29]. With knowledge of the scattering amplitude, a PRD could be calculated [1]. Since the DSD characteristics may change for different cases, it is better to use climatological DSD observations to obtain a robust SC relation among the polarimetric variables, which is expressed as

$$K_{\rm DP}(Z_h, Z_{\rm dr}) = CZ_h^{\alpha}Z_{\rm dr}^{\beta} \tag{6}$$

where Z_h and $Z_{\rm dr}$ are the linear forms of Z_H and $Z_{\rm DR}$, respectively. The parameters C, α, and β can be estimated by minimizing the sum of the squared errors of Z_h, $Z_{\rm dr}$, and $K_{\rm DP}$ from the equation. $K_{\rm DP}$ estimates can be acquired from measured Z_H and $Z_{\rm DR}$ with (6). It is worth noting that Z_H and $Z_{\rm DR}$ measurements suffer from attenuation in rain, miscalibration, partial beam blockages, and random fluctuations. Miscalibration, partial beam blockages, and attenuation should be corrected first [30]–[33] or corrected adaptively. The impact of random fluctuations can be reduced by applying moving median and mean filters.

In this method, the errors of $K_{\rm DP}$ estimates are attributed to the inaccuracy (or lack of representativeness) of the SC relation and the errors of measurements (i.e., Z_H, $Z_{\rm DR}$). A detailed error analysis is worthwhile but is beyond the scope of this paper. Estimates from self-consistency method with two different $Z_H/Z_{\rm DR}$ moving filters are compared in the succeeding section.

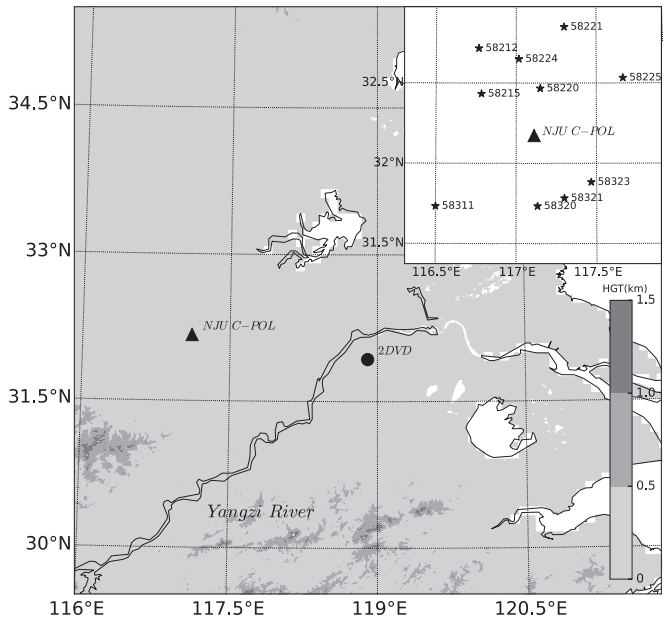

Fig. 1. Location and topography of Yangtze–Huaihe river basin and instruments sites. The black triangle and circle indicate NJU C-POL, 2DVD, respectively. Black pentagrams in the smaller subplot indicate AWS locations.

III. Ideal Experiment

A. Experiment Design

LSF, LP, and SC-based $K_{\rm DP}$ estimation methods are applied on a set of radial simulated PRD to illustrate the different characteristics of each method. These simulated PRD are based on a time series of DSD observation from a 2-D video disdrometer (2DVD), which is deployed at Nanjing City, Jiangsu Province, China, from a precipitation event on July 19, 2015. The position of the 2DVD is denoted on the topographic map in Fig. 1.

A constrained gamma model is used to process the DSD observations to generate the simulated data [34], [35], which is expressed by

$$N(D) = N_0 D^{\mu}\exp(-\Lambda D), \quad 0 \le D \le D_{\max} \tag{7}$$

where $N(D)$ is the raindrop number concentration of each size interval, D is the equivalent volume diameter (in millimeters), $D_{\max}$ is the maximum equivalent diameter of raindrops and is assumed 8 mm, N_0 is the number concentration parameter, μ is the shape parameter, and $\Lambda(\text{mm}^{-1})$ is another parameter of distribution. Since the constrained gamma model uses a statistical relation between the parameters μ and Λ, only two estimated DSD moments are needed to find the DSD parameters in (7).

First, the third (M_3) and sixth (M_6) moments of the DSD, i.e.,

$$M_n = \int_0^{D_{\max}} D^n N(D) dD \tag{8}$$

are estimated from observations [36]. Moving median and mean filters are used to filter out the high frequency fluctuations of moments. These fluctuations are mostly caused by the microscale variability of precipitation systems, the difference of sampling volume between disdrometer and radar, and the

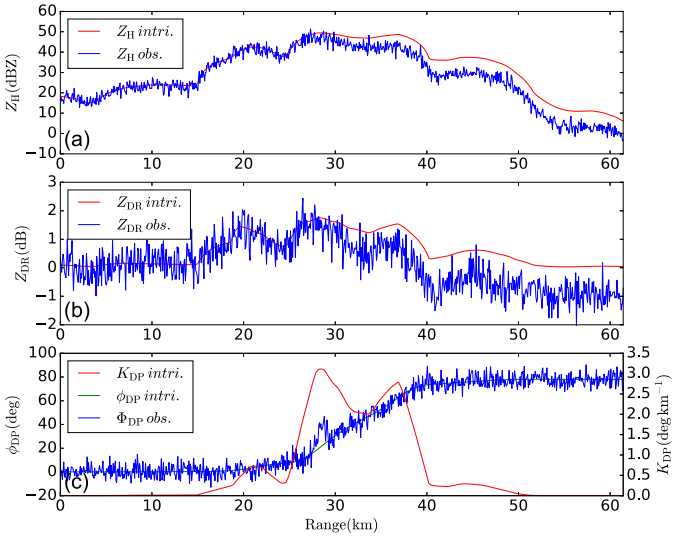

Fig. 2. Range profile of polarimetric variables from simulated DSDs. (a) Intrinsic Z_H (red solid line) and Z_H observation (blue solid line). (b) Intrinsic Z_{DR} (red solid line) and Z_{DR} observation (blue solid line). (c) Intrinsic K_{DP} (red solid line), Φ_{DP} observation (blue solid line), and intrinsic ϕ_{DP} (green solid line).

observation errors of disdrometer. After this procedure, M_3 and M_6 are linearly interpolated so that the simulated data can have a radial resolution of 75 m. We then use a method similar to the truncated moment fit method introduced by Vivekanandan *et al.* [36] to obtain DSD parameters (N_0, μ, and Λ), as

$$\begin{cases} \frac{M_6}{M_3} = \frac{N_0\Lambda^{-(\mu+7)}\Gamma(\mu+7)}{N_0\Lambda^{-(\mu+4)}\Gamma(\mu+4)} = \frac{\Gamma(\mu+7)}{\Lambda^3\Gamma(\mu+4)} = \frac{(\mu+6)(\mu+5)(\mu+4)}{\Lambda^3} \\ \mu = -0.024\Lambda^2 + 1.0662\Lambda - 2.7433 \\ N_0 = \frac{M_6\Lambda^{(\mu+7)}}{\Gamma(\mu+7)} \end{cases} \tag{9}$$

where the $\mu - \Lambda$ relation is obtained from DSD observations measured by 2DVD in 2014 and 2015, using the method of sorting and averaging based on two parameters (SATP) that was described by Cao *et al.* [37].

PRD including Z_H, Z_{DR}, K_{DP}, specific horizontal attenuation (A_H), and specific differential attenuation (A_{DP}) are calculated from the simulated DSD with the T-matrix method. The axis ratio of raindrops is set following the experimental fit [2]; the wavelength for these calculations is set as 5.33 cm, which is a typical value for C-band radar. The temperature is set to 10 °C. The range profile of intrinsic Z_H, Z_{DR}, K_{DP}, and ϕ_{DP} are shown in Fig. 2.

Random fluctuations, which commonly exist in measured Z_H, Z_{DR}, and Φ_{DP}, are represented by normally distributed random noise (white noise). The standard deviations of Z_H, Z_{DR}, and Φ_{DP} errors are assumed 2 dBZ, 0.4 dB, and 5°, respectively. The SNR influence on the random fluctuation is ignored for these calculations. To examine the impact of the backscattering phase caused by large raindrops or melting hail, the differential backscattering phase δ_{hv} is set to nonzero at the first K_{DP} peak in the vicinity of 28.5 km (called "bump" region), following

$$\delta_{hv}(r) = \begin{cases} \frac{300}{\sqrt{2\pi}\sigma_r}\exp\left[-\frac{(r-r_0)^2}{2\sigma_r^2}\right], & r_0 - 0.75\text{ km} < r \\ & < r_0 - 0.75\text{ km} \\ 0, & \text{else} \end{cases} \tag{10}$$

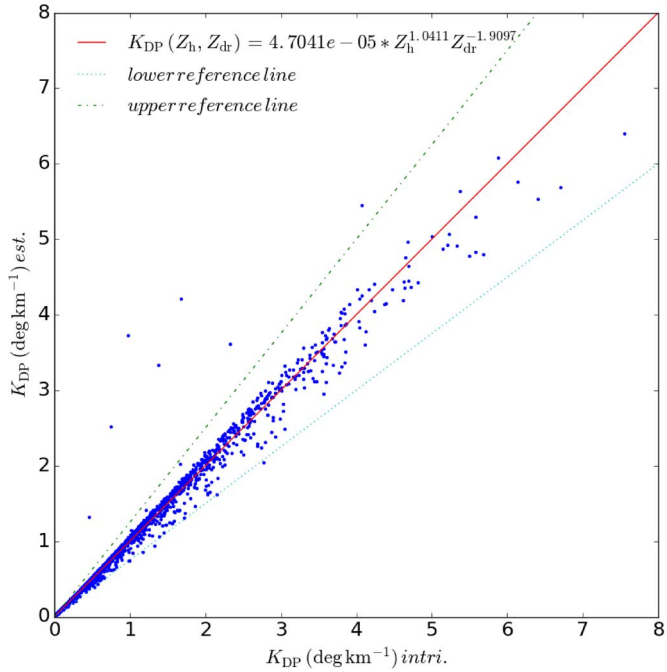

Fig. 3. Scattergram of simulated K_{DP} directly from 2DVD observation versus K_{DP} estimation from Z_H and Z_{DR} using a self-consistency relation. The DSD data used were collected by 2DVD denoted in Fig. 1 from 2014 to 2015. The green dot-dashed line and cyan dotted line are upper [125% $K_{DP}(Z_H, Z_{DR})$] and lower [75% $K_{DP}(Z_H, Z_{DR})$] reference lines.

where σ_r is the shape parameter (is assumed 8 km); r is the range distance from the radar (in kilometers); and r_0 is the center of the "bump." The large "bump" with a maximal differential backscattering phase of 15° occurs occasionally in real cases; it is used to inspect the performance of these K_{DP} estimation algorithms under this extreme situation. Finally, the intrinsic value, propagation effect, random fluctuations and "bump" effects in Φ_{DP} constitute the simulated measurements, following

$$\begin{cases} Z'_H(k) = Z_H(k) - 2\Delta r\sum_{i=1}^{k-1} A_H(i) + \varepsilon_{Z_H} \\ Z'_{DR}(k) = Z_{DR}(k) - 2\Delta r\sum_{i=1}^{k-1} A_{DP}(i) + \varepsilon_{Z_{DR}} \\ \Phi_{DP}(k) = \phi'_{DP}(k) = 2\Delta r\sum_{i=1}^{k-1} K_{DP}(i) + \delta_{hv} + \varepsilon_{\Phi_{DP}} \end{cases} \tag{11}$$

where the accumulation means the propagation effect of A_H, A_{DP}, and K_{DP}.

In Fig. 2, the whole range of the rain cell is about 60 km, with the most intense parts located from about 25 to 40 km. The largest K_{DP} value exceeds 3° per kilometer. Attenuation becomes significant, and Φ_{DP} increases rapidly through the intense parts of the rain cell. The large backscattering phase causes a large "bump" in the vicinity of the first peak of K_{DP}. For this region, it is obviously uneasy to estimate K_{DP} from Φ_{DP} because backscattering overruns the propagation effect. Nevertheless, the power measurements Z_H and Z_{DR} are relatively immune from the back scattering phase as long as there is no hail. The accuracy of K_{DP} estimates from the SC relation is mainly decided by the feasibility of the relation for a particular case, the random fluctuations of Z_H/Z_{DR} measurements, and the effect of attenuation in rain.

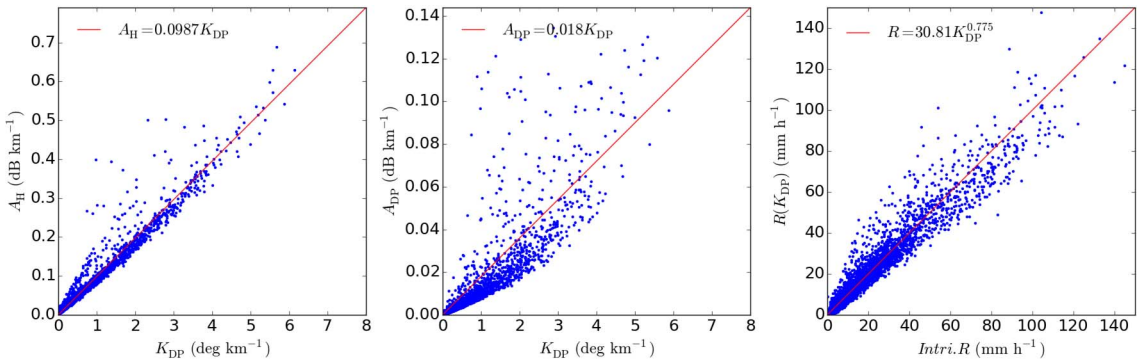

Fig. 4. Specific attenuation (A_H: left) and specific differential attenuation (A_{DP}: middle) versus specific differential phase (K_{DP}) for C-band, as well as the calculated intrinsic rain rate versus that estimated from K_{DP}.

B. Climatological Parameters

To obtain the parameters for the self-consistency, the two-year climatological DSD data from 2014 and 2015 observed by the same 2DVD as in the simulation section was used. The SC relation obtained with the method documented in the earlier section is shown in Fig. 3 as a scatter plot and expressed by

$$K_{DP}(Z_h, Z_{dr}) = 4.7041e^{-5} Z_h^{1.0411} Z_{dr}^{-1.9097} \tag{12}$$

with $Z_h = 10^{Z_H/10}$ in unit of mm^6 m^{-3} and $Z_{dr} = 10^{Z_{DR}/10}$, which is dimensionless. The scatters of intrinsic K_{DP} values, versus those estimated with (12), are distributed closely around the unity line except for several outliers. The DSDs of these outliers are dominated by a few of big drops, mainly due to the size sorting effect [38], [39] of wind shear, deviating from the standard gamma model. Even with all the different types of DSDs, the SC relation of PRD exhibits great reliability and robustness. To obtain the accurate parameters in (12), all fitting procedures in this paper are performed using nonlinear methods in a linear scale instead of simple linear fitting in logarithmic scale. This is because the linear fitting in logarithmic scale would enlarge the weights of smaller data values. As there are much more light rain samples from our DSD observation, the fitting results can bias to light rain in linear fitting in logarithmic scale.

In addition to the SC relation among PRD, the linear coefficients of $A_H - K_{DP}$ (c) and $A_{DP} - K_{DP}$ (d) are also regressed to be utilized in attenuation correction [31], written as $c = 0.0987$ and $d = 0.018$. The regression performance is shown in Fig. 4. With the coefficients c and d, attenuation of Z_H and Z_{DR} could be corrected with

$$\begin{aligned} Z_H &= Z'_H + c\Phi^U_{DP} \\ Z_{DR} &= Z'_{DR} + d\Phi^U_{DP} \end{aligned} \tag{13}$$

in which Φ^U_{DP} means the unfolded and nonfiltered differential phase, and Z'_H and Z'_{DR} indicate attenuated measurements.

C. Comparison of Results

The K_{DP} estimations of the simulated experiment with LSF, LP, and self-consistency systems are compared here. Different lengths of adaptive range, derivative filter, and moving window for LSF, LP, and self-consistency methods, respectively, are used to illustrate the impact of these parameters to the whole system. In Fig. 5(a), the adaptive range is 2 km/27 gates for $Z_H \geq 40$ dBZ and 6 km/81 gates for $Z_H < 40$ dBZ for LSF, the derivative filter is 2 km/27 gates for LP, and the moving window is 1 km/15 gates for self-consistency. A shorter moving window is used because the Z_H/Z_{DR} standard deviation is much smaller than that of Φ_{DP}.

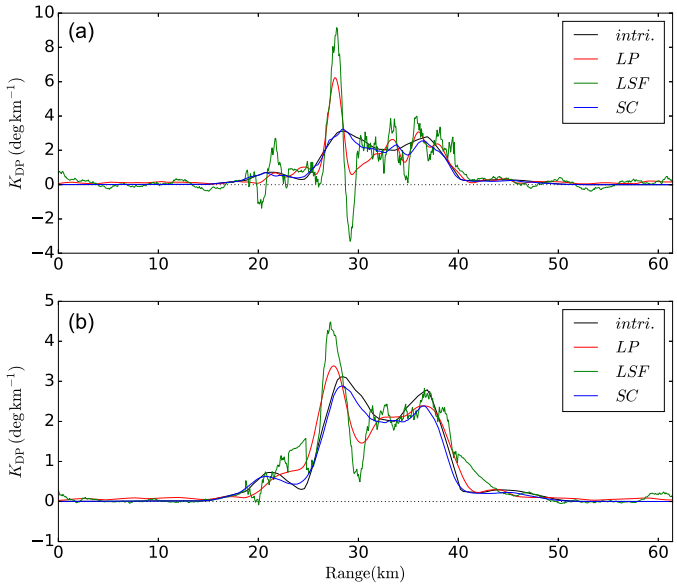

Fig. 5. Comparisons of K_{DP} estimations from the LSF (green solid), LP (red solid), and self-consistency (blue solid) methods with two different lengths of adaptive ranges/derivative filters/moving windows. Shorter (2 km) options as in (a), longer (6 km) options as in (b). The intrinsic K_{DP} is denoted with a black solid line.

The LSF-based K_{DP} estimations have the worst performance among these three methods. Due to the "bump" effect, K_{DP} estimations have very significant fluctuations near this region. The peak is higher than 9°/km and the valley at the "leeside" can be lower than −3°/km. This would lead to nonphysical QPE results. Even at the positions where the intrinsic values are less than 1°/km (meaning that the slope of ϕ_{DP} is insignificant), K_{DP} estimates can still be negative. Statistical errors are not handled well in the LSF approach. When LP is used, the results are better. First, due to the nonnegative constraint used, estimated K_{DP} values can never be negative even at the leeside of the "bump" region, where measured Φ_{DP} is of a downward trend. This is a substantial improvement since erroneous negative

values are completely avoided. Furthermore, $K_{\rm DP}$ values at the windward side are also better than those obtained from the LSF method because of the constraints used in the LP approach. LP also results in better $K_{\rm DP}$ estimates where the rain rate is low.

Not surprisingly, the SC $K_{\rm DP}$ estimation results in the best outcome for this experiment. In Fig. 3, the self-consistency of PRD is very reasonable. It is fair to say that $K_{\rm DP}$ is not completely independent from Z_H and $Z_{\rm DR}$ when the DSDs are not absolutely different from the climatology. In Fig. 5, the difference between $K_{\rm DP}$ estimates from the SC method and intrinsic values are quite small, particularly at the "bump" region. Differences exist only in the vicinity of the second $K_{\rm DP}$ peak. This is a nearly perfect result because the intrinsic self-consistency of simulated experiment PRD is almost identical to what we get from climatological DSD data (not shown), meaning that the model error is small. The main source of error is the random fluctuation, which is reduced by the moving filters. However, in other cases including real-world implementation, the model error due to the deviation of intrinsic self-consistency from the statistical relation would need to be taken into account.

Doubling the lengths of the adaptive ranges, the derivative filter and moving windows with respect to those in Fig. 5(a), we obtain another set of results, shown in Fig. 5(b). Generally, $K_{\rm DP}$ estimates are smoother when compared with those in Fig. 5(a). According to $\mathrm{SD}(K_{\rm DP}) = (\mathrm{SD}(\Phi_{\rm DP})/\sqrt{N(N-1)(N+1)/3})(1/\Delta r)$, the random errors of LSF $K_{\rm DP}$ estimates would decrease to about 1/3 of those in Fig. 5(a) [4], [40]. Therefore, the number of negative values decreases remarkably. However, at about 24 km, the values become abnormally large. This is mainly due to the incorporation of the "bump" part of the $\Phi_{\rm DP}$ profile when the lengths of adaptive range are enlarged. It is not surprising to see that values from LP do not show such a tendency because the consideration of the entire ray. The results from LP are also closer to the intrinsic values near the first peak. However, the results at the second $K_{\rm DP}$ peak are overly smoothed when compared with those in Fig. 5(a). The errors here are not as severe as the errors in the "bump" regions. Nevertheless, this highlights that uniform length derivative filters without additional constraints could either oversmooth the results when errors are not too severe, or undersmooth the results where $\Phi_{\rm DP}$ measurements are too "noisy." For this example, Z_H and $Z_{\rm DR}$ measurements are also smoother due to the increased length of the moving window in the SC estimation. The results are also overly smoothed in the figure.

The intrinsic differential phase and the error part of $\Phi_{\rm DP}$, including random fluctuation and nonzero differential backscattering phase, are segregated in the LSF and LP methods. $K_{\rm DP}$ estimated from LSF and LP may deviate from the intrinsic values when the information provided by the error part dominates compared with that provided by the intrinsic differential phase. The performance of $K_{\rm DP}$ estimation from measured polarimetric data depends mainly on to what degree the method can extract information provided by intrinsic differential phase from the measured data: The more the useful information is contaminated by the error, the worse the performance will be. In most $K_{\rm DP}$ estimation approaches, including LSF and the basic LP [17], only $\Phi_{\rm DP}$ measurements are used. Therefore, these methods may perform worse when they are applied on the data for which the information provided by error plays a more important role. The ratio of useful information to error mainly depends on the magnitude of the error in polarimetric measurements, and the scales (for matching fixed-length filters) over which these operate. This is related to many factors such as radar hardware (e.g., antenna design and transmitter characteristics), operating parameters (e.g., pulse repetition frequency or PRF), the propagation and scattering characteristics of the targets (e.g., Doppler spectrum characteristics), distance between targets and radar, and so on. Therefore, the performance of different methods also depends on the data. Likewise, only Z_H and $Z_{\rm DR}$ measurements are used in the self-consistency method. However, the SC relation in a specific case could deviate from the statistical one, and there are also errors in Z_H and $Z_{\rm DR}$ measurements. Therefore, it is natural to combine these methods together and to make use of as much information as possible. In the succeeding section, we will propose a hybrid method based on the combination of the LSF, LP, and SC $K_{\rm DP}$ estimation methods.

IV. Hybrid Method on the Ideal Experiment

According to information theory [41], as more information is used in appropriate ways, variables can be more accurately determined. Under the guidance of this principle, a hybrid method using all available measurements including Z_H, $Z_{\rm DR}$, and $\Phi_{\rm DP}$ is proposed based on the LP. $\rho_{\rm hv}$ usually decreases when radar scans across insects or clutters; thus, it is usually used to identify and remove nonmeteorological echoes.

As mentioned earlier, the SC $K_{\rm DP}$ estimation could obtain very accurate results when a proper moving filter is chosen. Although model errors could cause degradation in estimation accuracy, it is revealed in Fig. 3 that SC relation is very stable from a climatological perspective. In the hybrid method, the upper and lower limits for $K_{\rm DP}$ estimations are calculated from Z_H, $Z_{\rm DR}$, and $\Phi_{\rm DP}$ measurements with LSF, LP, and self-consistency as accurately as possible. Then, these reasonable upper and lower constraints for $K_{\rm DP}$ can be incorporated in the LP system. Such combinations of methods and measurements should be able to make better use of observational information and make $K_{\rm DP}$ estimates more accurately.

First, upper and lower limits are decided according to the upper and lower boundary shown in Fig. 3, following

$$\begin{aligned} K_{\rm DP}^{U} &= C^{U} \bullet K_{\rm DP}(Z_h, Z_{\rm dr}) \\ K_{\rm DP}^{L} &= C^{L} \bullet K_{\rm DP}(Z_h, Z_{\rm dr}) \end{aligned} \tag{14}$$

where $K_{\rm DP}^{U}/K_{\rm DP}^{L}$ and C^{U}/C^{L} mean the upper/lower $K_{\rm DP}$ limits and the slope of upper/lower boundary in Fig. 3, respectively. If radome attenuation or partial beam blockage exists in real cases, there exist biases in reflectivity measurements. The biases can be corrected from LP/LSF-estimated $K_{\rm DP}$ using methods similar to Vivekanandan *et al.* [20]. The moving windows used in this example are the shorter than those used in the SC method in Fig. 5(a). Limits from (14) only use Z_H and $Z_{\rm DR}$. To eliminate the potential effect of model error from the SC relation or of statistical error in measurements, these limits should be further adjusted with LSF-based $K_{\rm DP}$ estimations. LSF uses only $\Phi_{\rm DP}$ measurements so that those

estimates represent information purely independent from the SC relation. In this paper, heavily smoothed LSF estimations with adaptive ranges three times the length of those used in Fig. 5(a) are utilized. Adjusting the lower limits is as follows:

$$K_{\rm DP}^{L} = \begin{cases} 0.5K_{\rm DP}^{L} & \text{if } K_{\rm DP}^{(H)} < 0 \\ K_{\rm DP}^{(H)} & \text{if } 0 \le K_{\rm DP}^{(H)} < K_{\rm DP}^{L} \\ K_{\rm DP}^{L} & \text{if } K_{\rm DP}^{(H)} \ge K_{\rm DP}^{L} \end{cases} \tag{15}$$

where heavily smoothed $K_{\rm DP}$ estimates from LSF are denoted $K_{\rm DP}^{(H)}$. $K_{\rm DP}^{(H)}$ tends to underestimate $K_{\rm DP}$ values in heavy rain regions and overestimate those in the transition region between light rain and heavy rain. Equation (15) would eliminate abnormally low values in the lower limits. Overestimations in $K_{\rm DP}^{(H)}$ would not play any role in (15). The upper limits are adjusted as follows:

$$K_{\rm DP}^{U} = \begin{cases} 8, & K_{\rm DP}^{U} > 8, \text{ and } Z_H < 35 \text{ dBZ} \\ 10, & K_{\rm DP}^{U} > 10, \text{ and } Z_H < 45 \text{ dBZ}. \end{cases} \tag{16}$$

Information from LSF is not used here because it is not easy to obtain stable upper $K_{\rm DP}$ limits without super overestimations, and severe overestimations would cause negative consequence.

The combination of the LSF and self-consistency methods results in better lower and upper limits for the $K_{\rm DP}$ estimation. When errors dominate in $\Phi_{\rm DP}$ measurements, the lower limits mainly use information from Z_H and $Z_{\rm DR}$ measurements in the estimation. Similarly, the heavily smoothed LSF-based $K_{\rm DP}$ estimates will play a role when errors in Z_H and $Z_{\rm DR}$ measurements dominate. The errors in one measurement can be ameliorated by the useful information in the other measurements.

Since more accurate limits are obtained, the next step is combining them with the LP system. Equations (4) and (5) are modified to

$$\mathbf{A}_{\rm AUG} = \begin{pmatrix} \mathbf{I}_n & -\mathbf{I}_n \\ \mathbf{I}_n & \mathbf{I}_n \\ \mathbf{Z}_{n-(m-1)/2,n} & \mathbf{M}_{n-(m-1)/2,n} \\ \mathbf{Z}_{n-(m-1)/2,n} & -\mathbf{M}_{n-(m-1)/2,n} \end{pmatrix} \tag{17}$$

$$\mathbf{b}_{\rm AUG} = \left(-\mathbf{b}, \mathbf{b}, \mathbf{K}_{\mathbf{DP}}^{\mathbf{L}}, -\mathbf{K}_{\mathbf{DP}}^{\mathbf{U}}\right)^{T} \tag{18}$$

respectively. Now, $K_{\rm DP}$ constraints are controlled by the modified augmented part of $\mathbf{A}_{\rm AUG}$ and $\mathbf{b}_{\rm AUG}$, which can be written as $\mathbf{K}_{\mathbf{DP}}^{\mathbf{L}} \le \mathbf{M}_{n-(m-1)/2,n}\mathbf{x} \le \mathbf{K}_{\mathbf{DP}}^{\mathbf{U}}$, instead of simplified monotonicity constraints (nonnegative $K_{\rm DP}$) used in the original LP method.

We call this approach a hybrid method not only because it is the combination of the equations of the LSF, LP, and self-consistency methods but also for blending the underlying philosophy for each of them. The LSF is the most straightforward method. It can result in a satisfactory $K_{\rm DP}$ estimation when the error in the measurements does not dominate. The LP method is a global optimization algorithm for $\phi_{\rm DP}$. However, the basic methods implemented to shorter wavelengths lack some detailed consideration for $K_{\rm DP}$ estimation realities, particularly when the error in $\Phi_{\rm DP}$ overruns the useful information. The self-consistency method previously designed for partial beam blockage and other corrections capitalizes better on other available information (Z_H and $Z_{\rm DR}$). This self-consistency approach often fails in critical situations such as hail cores where these methods must rigidly adhere to consistency relationship constraints that do not apply.

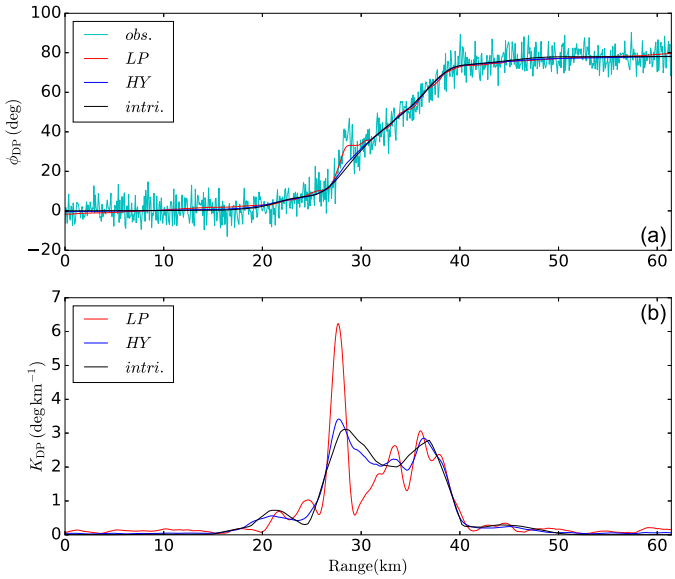

Fig. 6. Comparisons of (a) $\phi_{\rm DP}$/ (b) $K_{\rm DP}$ estimates from the hybrid (blue solid) and basic LP (red solid) methods. Simulated $\Phi_{\rm DP}$ observations are denoted as cyan solid line in (a). The intrinsic $\phi_{\rm DP}/K_{\rm DP}$ values are denoted with black solid lines.

The proposed hybrid method and the original LP method are applied on the simulated data to show the changes in the performance (see Fig. 6). The derivative filters are set as 2 km in length for both. There is only a marginal difference between $\phi_{\rm DP}$ estimates from the two methods when taking an overall view of whole radial data. $K_{\rm DP}$ estimated by the hybrid method is smoother and much closer to intrinsic $K_{\rm DP}$, due to the more accurate constraints from the additional information. As described earlier, the lower the ratio of information provided by the intrinsic differential phase and the error, the more difficult it is to find solutions close to the intrinsic variables. The difference between solutions estimated by the hybrid method and the original LP method reach a maximum at the "bump" region where the information ratio is the lowest. In the "bump" regions, minor useful information is provided by $\Phi_{\rm DP}$ measurements; therefore, constraints play relatively important roles. When the LP method is used without additional constraints, the nonnegative constraints associated with the cost function (of minimizing difference between measured and filtered differential phase) would make $\phi_{\rm DP}$ increase quickly along with the upward slope part of the 'bump' region as shown by the red line in Fig. 6(a) and then increase slowly in the remaining part of the "bump." This would result in abnormally large $K_{\rm DP}$ values in the upward slope part and abnormally low $K_{\rm DP}$ values in the remaining part. When additional information is used as upper and lower constraints in this hybrid method, $K_{\rm DP}$ is limited by stricter constraints than the simpler nonnegative constraint. We see that upper and lower constraints from extra Z_H and $Z_{\rm DR}$ measurements result in a better estimation than simple nonnegative physical constraints.

TABLE I
SETTINGS AND PARAMETERS OF NJU C-POL AND ITS OBSERVATIONS

Parameters	NJU C-POL（mobile）
Transmitter	5.625 GHz （klystron）
PRF	1000 Hz
Pulse width	0.5 μs
Peak Power	> 250 kW
Receiver	Simultaneous Horizontal/Vertical
Noise figure	< 3 dB（H and V channel）
Dynamic range	> 95 dB
Antenna feeder	paraboloid，center feed
Antenna gain	> 41 dB
Antenna aperture	3.2 m
Beam width	1.2°
Sidelobe	< -40 dB (> 15°)
Polarimetric mode	Simultaneously transmit and receive H and V
Scanning mode	PPI: 0-360° rotating speed: ~15°s^{-1} time for VCP: ~6min
Elevations	0.5, **1.5**, 2.4, 3.4, 4.3, 5.3, 6.2, 7.5, 8.7,10.0, 12.0, 14.0, 16.7, 19.5, **90.0**
Precision	
Radial resolution	75m
Radar variables	Z_H, Z_{DR}, ρ_{hv}, Φ_{DP}, v_r, σ_v, SNR
Z_H precision	1 dB
v_r precision	1 m/s
σ_v precision	1 m/s
Z_{DR} precision	0.2 dB
Φ_{DP} precision	2°

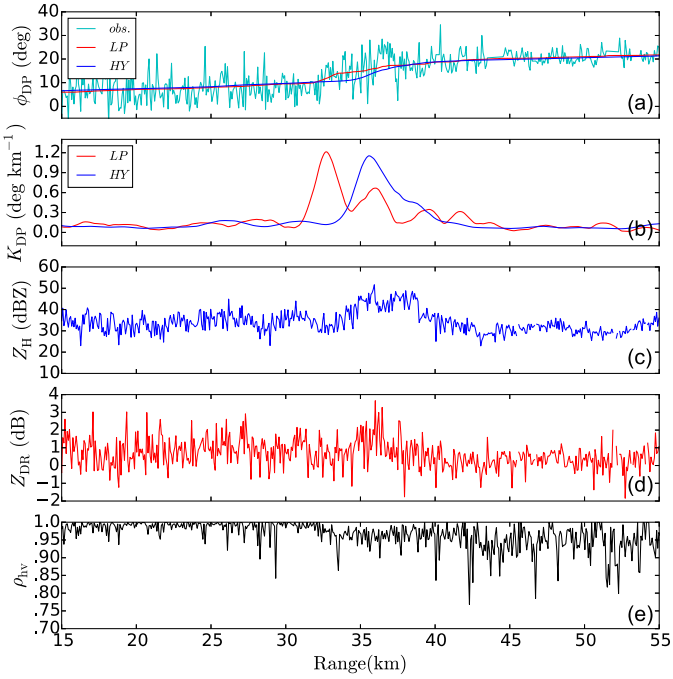

Fig. 7. Comparisons of (a) ϕ_{DP}/ (b) K_{DP} estimates from hybrid (blue solid) and basic LP (red solid) methods applied on a ray collected by NJU C-POL on July 11, 2014 at 23:25 UTC at an elevation of 1.5° and azimuth of 54.33°. Φ_{DP} observations are denoted the cyan solid line in (a). The attenuation corrected Z_H (blue solid), attenuation corrected Z_{DR} (red solid), and corrected ρ_{hv} (black solid) are denoted in subplots (c), (d), and (e).

V. VERIFICATION WITH A REAL CASE

The Nanjing University C-band Polarimetric Radar (NJU C-POL) is a mobile C-band polarimetric radar for weather research, jointly designed by Nanjing University and Beijing Metstar Radar Company in China. Its main parameters are listed in Table I. During the 2014–2015 field campaign of Observation, Prediction, and Analysis of severe Convection of China (OPACC), NJU C-POL was deployed in Anhui Province, China, to observe the summer severe convection (see Fig. 1). An absolute calibration using a metallic ball was conducted to guarantee the accuracy of Z_H/Z_V before the observations. A vertically pointing scan was also performed every 6-min volume scan for Z_{DR} calibration. The distance between NJU C-POL and 2DVD is 171 km. These two instruments are influenced by the same synoptic systems. Therefore, it is acceptable to use DSD data collected by the 2DVD as representative to fit a statistical SC relation for NJU C-POL for application of the hybrid method on the measured PRD.

An event during the Intensive Observing Period 8 (IOP8) on July 11–12, 2014 is selected for investigation from the OPACC data set. To show the performance on the real event, the LSF/LP/hybrid K_{DP} methods will be applied on a plane position indication (PPI) scan. Then, QPEs from three sets of LSF, LP, and hybrid-based K_{DP} estimators will be compared with AR observed by several automatic weather stations (AWSs) within the observing umbrella of the radar. QPEs are estimated according to the $R - K_{DP}$ relation obtained from the 2DVD [8], [42], as shown in Fig. 4.

Radar scans at 1.5° instead of the lowest elevation (0.5°) are used to avoid the impact of partial beam blockages. The quality of radar moment data are carefully controlled with five procedures before estimating ϕ_{DP} and K_{DP}.

1) Z_H is calibrated according to the absolute calibration experiment.
2) Systematic differential phase in measured Φ_{DP} and Z_{DR} bias are removed with data from the vertical pointing scan.
3) The echoes having ρ_{hv} less than 0.75 or spectral width is larger than 9 m/s are considered nonmeteorological or second trip echo and thus removed.
4) A much stricter constraint is used to deal with Φ_{DP} measurements that may cause errors. Along all radials, if the Φ_{DP} difference between two adjacent gates is larger than 40°, ρ_{hv} is less than 0.9, or if the spectral width is larger than 6 m/s, the gate is flagged as a bad gate. Φ_{DP} values at these potential bad gates are removed and then refilled with the linear interpolations from the surrounding gates.
5) Finally, Φ_{DP} is unfolded, and correction for attenuation in rain for Z_H/Z_{DR} fields is conducted using (13).

To illustrate the difference of the hybrid method and the basic LP method, a comparison of their results on a radial data from a PPI image collected by the NJU C-POL on July 11, 2014 at 23:25 UTC is shown in Fig. 7. As influenced by the backscattering phase and noise, the observed Φ_{DP} increases abnormally near 35 km, which is called a "bump" region similar to the abnormal back scattering region in the ideal case. ρ_{hv} (denoted in subplot [e]) also manifests a decreasing tendency in this region. This "bump" region lacks sufficient differential phase information, which could obviously impact the

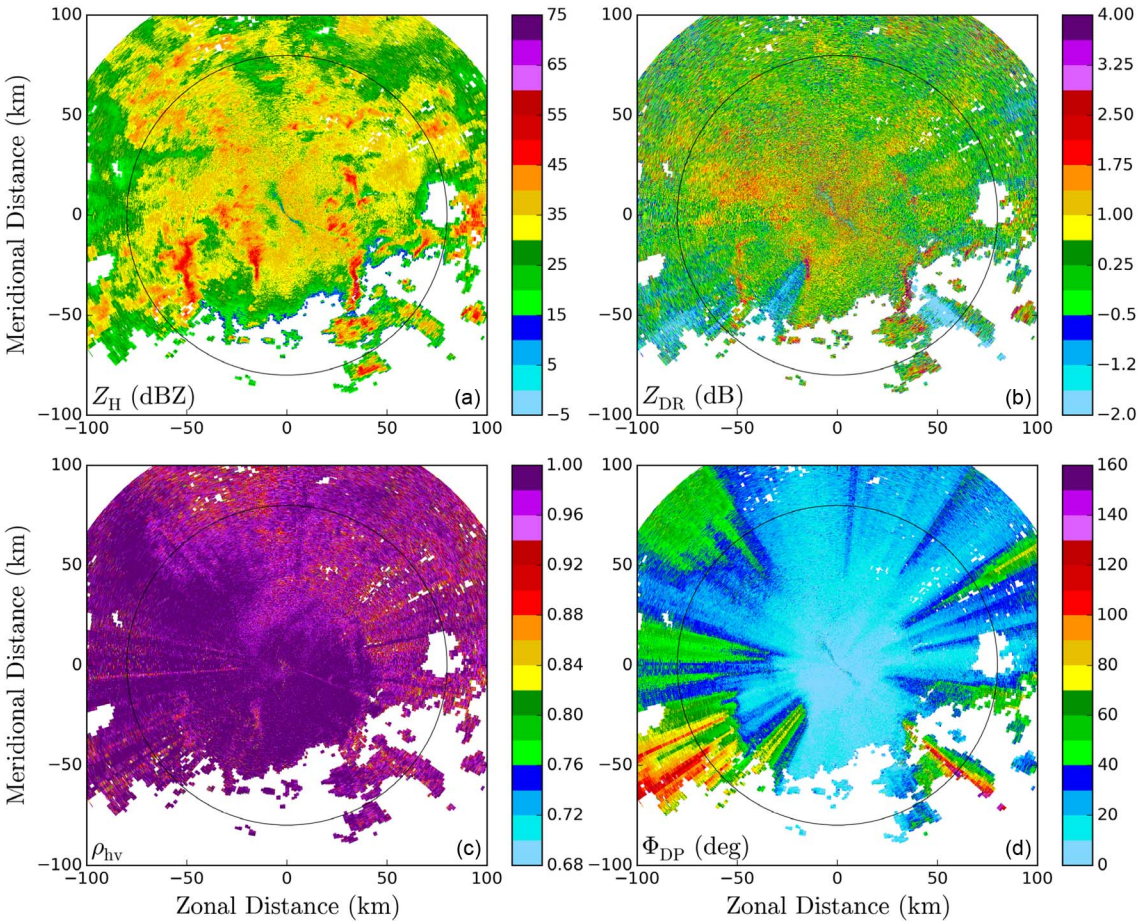

Fig. 8. Quality-controlled PRD images of a Meiyu precipitation event collected by NJU C-POL on July 11, 2014 at 23:25 UTC at an elevation angle of 1.5°. (a) Z_H (dBZ), (b) $Z_{\rm DR}$ (dB), (c) $\rho_{\rm hv}$, and (d) $\Phi_{\rm DP}$ (degrees).

performance of both methods. Similar to the results in the ideal case, the $\phi_{\rm DP}$ estimate from the LP method tends to increase rapidly at the first half part of the "bump" region and then to flatten afterward. This result is mainly required by the algorithm to minimize the cost function. However, due to the inclusion of physical constraints, the $K_{\rm DP}$ estimate from the hybrid method corresponds better with Z_H and $Z_{\rm DR}$ observations in subplots (c) and (d). It is very important to note that the frequency of the occurrence of such large "bump" features is not very low particularly in the C-/X-band radar data sets. As we tested in the real data, the inclusion of these physical constraints can obviously improve the quality of the $K_{\rm DP}$ estimates and rainfall estimates consequently. This will be further illustrated using the whole PPI image and QPE results.

The PPI image at the 1.5° elevation (see Fig. 8) shows that this Meiyu precipitation has a large region of uniform stratiform precipitation with multiple embedded convections near the southern part of the system. These embedded convections cause a significant radial $\Phi_{\rm DP}$ increase, corresponding to increased $K_{\rm DP}$ values. Since $\Phi_{\rm DP}$ measurements have a large dynamic range in the image, $\Phi_{\rm DP}$ is noisy and unsuitable for use in quantitative applications.

After quality control, $K_{\rm DP}$ values are estimated using the LSF method with the same adaptive ranges used in the algorithms of WSR 88D (2 km/6 km) and with LP/hybrid method with adaptive derivative filters of 27 gate lengths (2 km). Before estimating the upper and lower limits for the hybrid method, the attenuation-corrected $Z_H/Z_{\rm DR}$ are smoothed with 15-gate moving median and mean filters. Results from the PRD are found in Fig. 9. The most obvious difference of LSF-based $K_{\rm DP}$ estimates and LP/hybrid-based ones are that, with non-negative constraints in the LP method and SC constraints in the hybrid method, negative $K_{\rm DP}$ values completely disappear. Negative $K_{\rm DP}$ values are associated with localized errors. As proposed by Ryzhkov and Zrnić [8], QPE biases could be partially mitigated by including these negative rain rates associated with negative $K_{\rm DP}$ values. However, if the AR is not calculated over a sufficiently large spatiotemporal area to capture both negative and positive $K_{\rm DP}$ estimates, this may still result in a negative rainfall accumulation. Results of LP estimation seem to be much more capable than those from LSF estimation, with erroneous negatively values disappearing. However, as shown in Fig. 10(c) and (d), the original LP-based $K_{\rm DP}$ estimates near echo edges occasionally spike if backscatter phase contributions and filter length choices are not well handled. The results look improved in $K_{\rm DP}$ estimates using the hybrid method constraints as in Fig. 10(a) and (b) for those edge regions. Around the regions of embedded convection, where $\Phi_{\rm DP}$ measurements would likely increase more rapidly, there are additional azimuthal discontinuities in the $K_{\rm DP}$ image

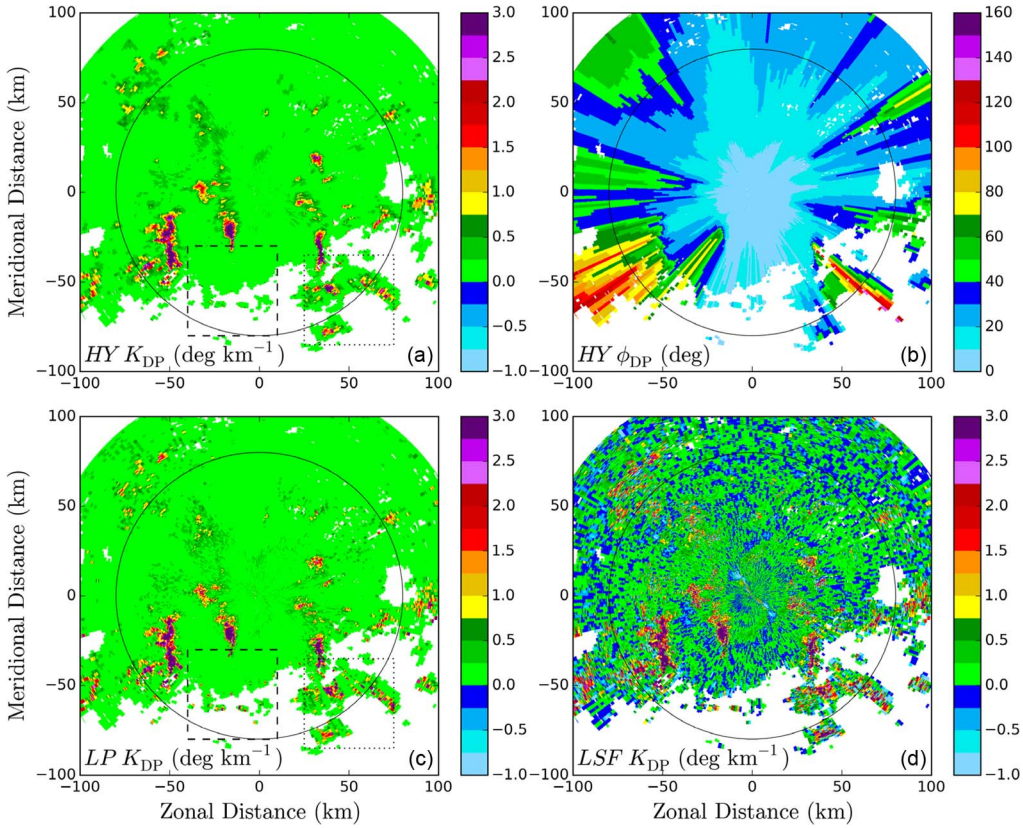

Fig. 9. Comparison of K_{DP}/ϕ_{DP} estimation based on NJU C-POL data shown in Fig. 8. (a) K_{DP} Estimates from hybrid method. (b) ϕ_{DP} Estimates from hybrid method. (c) K_{DP} Estimates from the basic LP method. (d) K_{DP} Estimates from the LSF method. The black circles are reference lines at a radius of 80 km from the radar. Regions denoted by dashed and dotted rectangles are enlarged in Fig. 10.

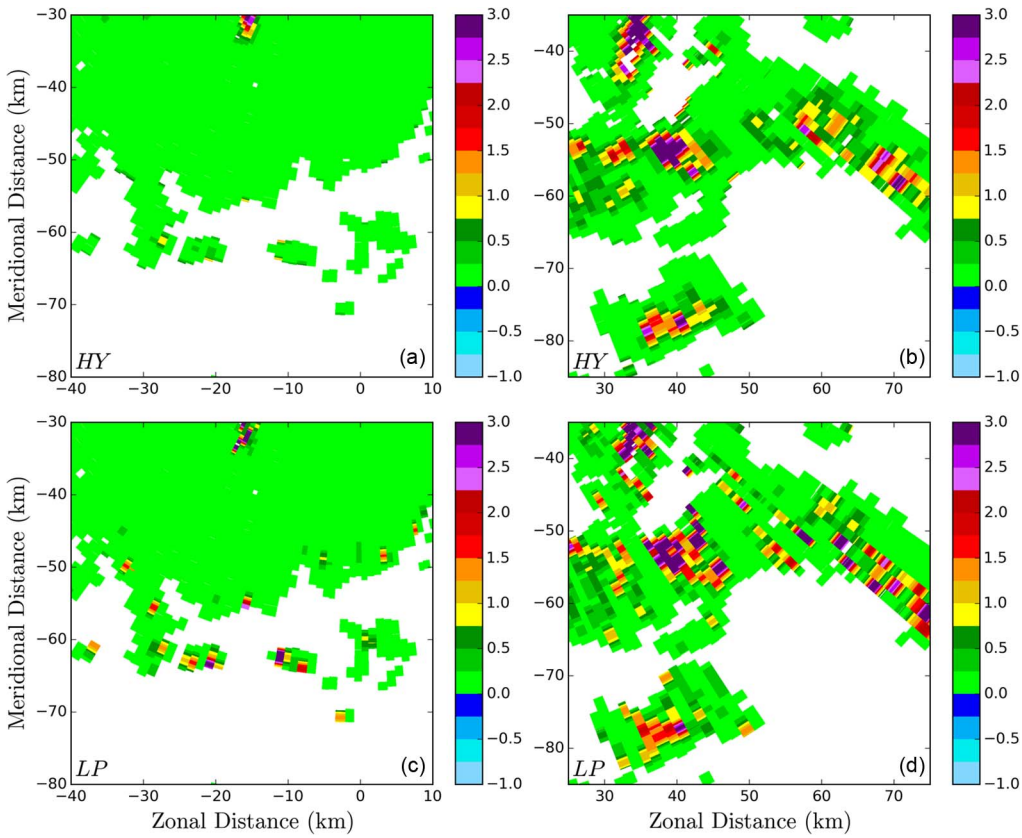

Fig. 10. Zoom in for K_{DP} images shown in Fig. 9. Region of (a)/(b) is corresponding to the dashed/dotted rectangle in Fig. 9(a); region of (c)/(d) is corresponding to the dashed/dotted rectangle in Fig. 9(c).

TABLE II
AWSs POSITIONS AND THEIR DISTANCES AWAY FROM NJU C-POL. THE FIRST LINE STANDS FOR THE NAMES OF THE AWSs

Station Name	58221	58225	58212	58215	58220	58224	58311	58320	58321	58323
Lon.	117.30	117.67	116.77	116.78	117.15	117.02	116.50	117.13	117.30	117.48
Lat.	32.85	32.533	32.717	32.433	32.467	32.65	31.73	31.733	31.78	31.88
Dis.	77.09	65.73	68.45	42.30	32.73	53.62	75.68	48.83	46.75	46.44

TABLE III
COMPARISON OF THE ACCUMULATED RAINFALL AR FROM AWS UNITS TO THOSE ESTIMATED FROM LSF/LP/HYBRID METHODS. INFORMATION ON THESE AWS STATIONS IS SHOWN IN TABLE II

Station Name			58221	58225	58212	58215	58220	58224	58311	58320	58321	58323
Total AR.		aws	39.70	42.80	44.30	40.40	39.90	36.90	72.80	21.90	26.60	41.80
		LSF	13.16	27.98	55.36	52.14	46.98	45.14	61.35	19.60	-9.86	24.31
		LP	35.20	34.12	44.97	57.30	69.75	43.42	57.05	29.35	26.78	36.70
		HY	38.47	34.95	53.39	53.09	63.51	46.52	65.63	23.06	23.33	41.45
CORR. COEF.	Rad.	LSF	0.41	0.45	0.42	0.52	0.41	0.66	0.51	0.00	0.19	0.31
		LP	0.60	0.56	0.73	0.72	0.57	0.89	0.57	0.48	0.34	0.48
		HY	0.75	0.66	0.88	0.83	0.71	0.94	0.61	0.81	0.60	0.39
	15 min	LSF	0.74	0.60	0.76	0.68	0.63	0.69	0.64	0.21	0.22	0.50
		LP	0.85	0.73	0.95	0.83	0.77	0.90	0.66	0.61	0.53	0.66
		HY	0.92	0.83	0.98	0.89	0.89	0.95	0.72	0.90	0.79	0.51
	30 min	LSF	0.80	0.78	0.88	0.77	0.70	0.75	0.65	0.20	0.31	0.79
		LP	0.89	0.83	0.98	0.88	0.84	0.90	0.67	0.70	0.71	0.87
		HY	0.95	0.91	0.98	0.94	0.91	0.95	0.72	0.93	0.87	0.80
	60 min	LSF	0.85	0.90	0.85	0.80	0.76	0.75	0.94	0.24	0.20	0.86
		LP	0.93	0.91	0.96	0.92	0.89	0.91	0.94	0.84	0.77	0.91
		HY	0.95	0.96	0.98	0.96	0.93	0.97	0.97	0.97	0.88	0.98
	180 min	LSF	0.91	0.92	0.80	0.95	0.91	0.80	0.93	0.65	0.10	0.90
		LP	0.95	0.94	0.97	0.98	0.97	0.93	0.97	0.94	0.89	0.93
		HY	0.96	0.97	0.96	0.99	0.98	0.98	0.97	0.99	0.95	0.99
RELATIVE ERROR	Rad.	LSF	2.64	2.40	2.68	2.61	3.15	2.21	2.94	4.84	3.36	3.26
		LP	1.68	1.76	1.67	1.31	1.44	1.07	2.24	1.88	2.01	2.46
		HY	1.38	1.28	1.14	0.79	1.05	0.90	2.06	1.00	1.42	3.29
	15 min	LSF	1.52	1.66	1.47	1.46	2.17	1.40	1.74	3.26	2.72	2.20
		LP	1.21	1.22	0.75	0.91	1.09	0.79	1.52	1.57	1.60	1.65
		HY	1.06	0.89	0.51	0.63	0.75	0.64	1.34	0.83	1.20	2.30
	30 min	LSF	1.37	1.04	1.07	1.20	1.69	1.12	1.30	3.09	2.50	1.39
		LP	1.14	0.93	0.58	0.83	0.91	0.71	1.15	1.34	1.44	1.04
		HY	0.99	0.67	0.44	0.53	0.68	0.58	1.04	0.71	1.14	1.27
	60 min	LSF	0.99	0.64	0.89	1.24	1.24	1.00	0.59	2.39	2.45	1.31
		LP	0.68	0.58	0.53	0.85	0.74	0.65	0.51	1.07	1.31	1.07
		HY	0.60	0.45	0.41	0.53	0.6	0.49	0.36	0.53	1.09	0.64
	180 min	LSF	0.95	0.50	0.69	1.01	0.76	0.88	0.50	1.69	2.43	1.06
		LP	0.61	0.46	0.32	0.83	0.55	0.67	0.35	0.83	1.02	0.73
		HY	0.57	0.34	0.34	0.48	0.47	0.55	0.33	0.37	0.81	0.35

from the lesser constrained LP method than that from the better constrained hybrid method. This azimuthal discontinuity (e.g., one not the direct result of rain microphysics) indicates a potential drawback for lesser constrained LP methods. In the meantime, having more realistic physical constraints under the proposed hybrid method, K_{DP} estimates seem to be more physically realistic and smoother.

Within 80-km radius of the NJU C-POL radar station, there are ten AWS locations with rain gauge measurements (positions as shown in Fig. 1). The distances between AWSs and the radar are listed in Table II. ARs from these AWSs are sampled at 1-min temporal resolution. Since the AWSs have much shorter sampling times than the radar (approximately 6 minutes), this allows a quantitative comparison at the radar observation scale temporal resolution. The total AR results for each AWS during this event are located in Table III. Most of the sites record moderate rainfall to heavier rainfall, with the largest 48-h AR recorded as 72.8 mm.

To quantify the precision of K_{DP} from the LSF/LP/hybrid methods, time series, $K_{\mathrm{DP}}(i)$, $1 \leq i \leq N$, over the AWSs' sites are extracted from estimates over the entire event from UTC 02:20, July 11, 2014 to UTC 23:50, July 12, 2014. With

these estimated K_{DP} time series, three sets of rain-rate series are estimated using the following:

$$R(i) = 30.81\left|K_{\mathrm{DP}}(i)\right|^{0.775}\mathrm{sign}\left[K_{\mathrm{DP}}(i)\right], 1 \le i \le N \quad (19)$$

where $R(i)$ is the rain rate at the ith scan. The parameters of (19) are estimated from the same data set as in Fig. 3. The scattergram of the fitting result is shown in Fig. 4. Then, the AR for each station is estimated as follows:

$$AR(i) = \begin{cases} R(i-1)\Delta t(i), & 2 \le i \le N \\ 0, & i = 1 \end{cases} \quad (20)$$

where $\Delta t(i)$ is the time interval between the ith and $i+1$th scans over the station. It is important to note that these time series report at the highest temporal resolution that we can obtain from the radar. Next, AWS observations and radar estimates are compared at five different temporal resolutions, including: 1) at the radar scan time; 2) every 15 min; 3) every 30 min; 4) every 60 min; and 5) every 180 min. Here, the time series at the coarser temporal resolution reflect integrations of those at the finest temporal resolution.

Correlation coefficients and relative errors, whose formulas are

$$\rho = \frac{\sum_{i=1}^{N}\left[AR_{\mathrm{AWS}}(i) - \overline{AR_{\mathrm{AWS}}}\right]\left[AR_{\mathrm{radar}}(i) - \overline{AR_{\mathrm{radar}}}\right]}{\sqrt{\sum_{i=1}^{N}\left[AR_{\mathrm{AWS}}(i) - \overline{AR_{\mathrm{AWS}}}\right]^2 \sum_{i=1}^{N}\left[AR_{\mathrm{radar}}(i) - \overline{AR_{\mathrm{radar}}}\right]^2}} \quad (21)$$

$$\varepsilon_r = \frac{\sqrt{\frac{1}{N}\sum_{i=1}^{N}\left[AR_{\mathrm{AWS}}(i) - AR_{\mathrm{radar}}(i)\right]^2}}{\frac{1}{N}\sum_{i=1}^{N} AR_{\mathrm{AWS}}(i)} \quad (22)$$

where AR_{AWS} and AR_{radar} are AR time series of a particular temporal resolution, and "$-$" denotes expected value, which are listed in Table III. The relative error represents to what degree the estimates deviate from the AWS observations. The AWS total ARs and K_{DP}-based estimates are also listed to show the absolute bias.

From the table, performance varies from station to station. These differences are because of several factors, including different sampling volume/time between the radar and AWSs, and the variability of precipitation when falling (e.g., as related to microphysical or dynamical processes). Not surprisingly, radar-estimated AR from all three methods is in better agreement with AWS observations at the coarser temporal resolutions. In general, estimates from the hybrid method correlate better with the AWS observations than do those from the basic LP method and the LSF approach. Once again, differences between the methods are less noticeable at coarser temporal resolution. Typically, rainfall comparisons between radar and *in situ* gauge measurements are produced at a temporal resolutions of 1-h or longer (e.g., 24-h daily accumulation mapping) to reduce the role of instantaneous measurement noise [2], [3], [42]. At such longer temporal resolutions, we find that correlation coefficients between the AR series and AWS observations are high, with most of them exceeding 0.95. It is shown in Table III that, even when the comparisons are made at the highest temporal resolution (radar scan time), the majority of the correlation coefficients between the AR time series and AWS observations are larger than 0.8. Additional information from Z_H and Z_{DR} included in the hybrid method makes such precise rainfall estimation possible. In contrast, the LSF method shows a significant deficiency. Most sets of rainfall estimates from the LSF method have extremely low correlation coefficients with AWS observations. Relative errors, which denote a relative magnitude of bias, still decrease when the comparison is conducted at a coarser temporal resolution. Finally, rainfall estimates from the hybrid method exhibit a lower bias than those from the other methods.

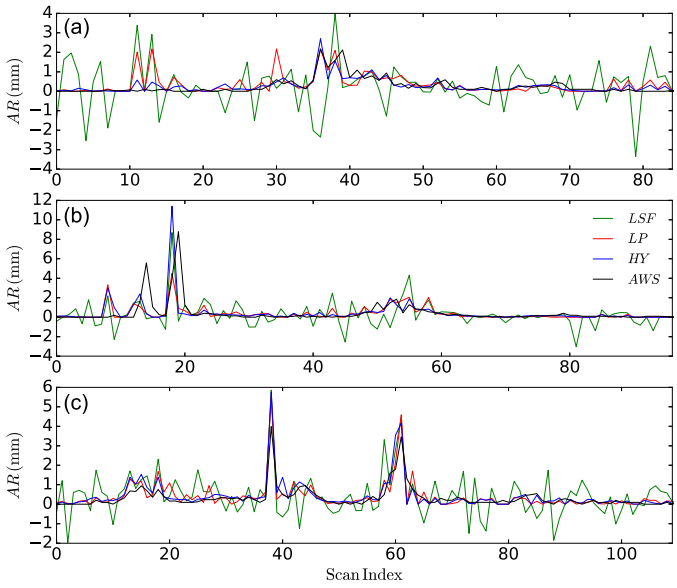

Fig. 11. Time series of AR estimated from K_{DP} of LSF (green solid lines), LP (red solid lines), and hybrid (blue solid lines) methods and corresponding AWS observations at stations (a) 58320, (b) 58323, (c) 58224.

Not surprisingly, a mismatch of the radar data and estimation methods and errors associated with the AWS observations would cause the differences between radar estimated rainfall and AWS observations. Three time-series traces from AWS observations (stations 58320, 58323, and 58224) and their corresponding radar rainfall estimates are selected to help illustrate the reasons associated with: 1) the LSF method underperforming as compared with the hybrid method; 2) rainfall estimations from all methods performing poorly; and 3) rainfall estimations from all three methods performing well. These time series examples to follow are all reporting at the native radar scan time interval.

To begin, Fig. 11 confirms that only those time series K_{DP} estimates from LSF methods report negative values. The underlying philosophy for including negative rainfall is that effect of erroneous negative K_{DP} values would be eliminated when spatial integration is calculated (as LSF methods would also promote compensating positive K_{DP} excursions); in other

words, spatial integration of $K_{\rm DP}$ values estimated from the LSF method would be close to the intrinsic value. If negative $K_{\rm DP}$ values (along a radial or along adjacent radials) are abandoned or absolute values are used, spatial integration would be positively biased. However, for these examples, time series performances over point locations are considered instead of wider spatial integrations. These negative rainfall values from the LSF would therefore be strongly decorrelated with the time series of the real precipitation. Fig. 11(a) highlights one example when the correlation coefficient of the LSF-method-based rainfall estimates with AWS observations for station 58320 is near 0, implying these estimates are strongly uncorrelated. For this station example, the peak of AR observations is not very large compared with the other two subplots. The magnitude of the oscillation of the LSF-method-based rainfall estimates exceeds the peak of AR observations. This means that the statistical noise resulting from the raw measurements and the processing algorithm completely contaminates the useful information.

For the LP method, the exclusion of extreme negative or positive excursion values makes the $K_{\rm DP}$ series correlations align closer to the intrinsic ones. However, the LP method cannot accurately recover $K_{\rm DP}$ at the "bump" regions with only its basic constraint configuration. Thus, we find that the extra physical constraints from Z_H and $Z_{\rm DR}$ have a positive effect for the hybrid-method-estimated $K_{\rm DP}$/rainfall time series. Overall, the hybrid method does a superior job when compared with the LSF and LP methods. For example, in the vicinity of index 12, both the rainfall estimates from LSF and LP predict two phantom peaks of AR, which do not match with the observations or the results from the hybrid method. The best performance in terms of total accumulation estimation is found for station 58323, where the total AR from hybrid method is almost equal to that from the observations.

However, despite the accurate AR estimate over longer scales for the hybrid method, the station 58323 example highlights other sources for the possible failure of all three methods at shorter scales including: 1) the phantom peak of AR near index 8; 2) the insufficient AR near index 12; and 3) the time shift of the main rainfall peak. As noted earlier, temporal mismatch issues are often related to mismatches between the height of the radar volume and the surface AWS station. This offset could be associated with instantaneous measurement errors from additional storm advection or drop distribution evolution. Several of these storm evolution factors may be offset if our comparisons are conducted over a coarser temporal resolution. For example, the correlation coefficients exceed 0.8 for all methods once we consider 1-h accumulations; the hybrid method-based AR reaches 0.98 for station 58 323. For station 58 224, the two AR peaks at indexes 38 and 60 are estimated successfully by all methods; thus, we are able to achieve decent correlation coefficients at both the high and coarse temporal resolutions across all methods.

Finally, it should be mentioned that the comparisons performed at station 58 321 were unexpectedly poor. The relative error (correlation coefficient) is extremely high (low), even when the comparison is conducted at the lengthier temporal scales, with emphasis on the LSF-method-based AR performance. The total LSF-method-based AR is -9.86 mm, and a negative 48-h AR is clearly not acceptable. As previously noted, spatiotemporal integration would potentially eliminate most detrimental effects of instantaneous LSF negative and positive value excursions. In general, our results still confirm the expectation that the longer the $K_{\rm DP}$ time series, the more likely we would find a result for the total AR close to the intrinsic value. In this example, the number of radar samples during the 48-h window is approximately 394, which is still insufficient to offset those negative values. Both the LP and hybrid methods perform poorly, but the hybrid method-estimated total ARs still suggest the lowest biases.

In general, the hybrid method performs better than the LSF/LP methods when applied to a real event, particularly when quantitatively compared verified with AWS observations.

VI. Discussion and Summary

To examine the performance of $K_{\rm DP}$ estimators for polarimetric radar measurements, LSF (which is the most common operational method), LP (which is a newly proposed optimization approach to guarantee the nonnegativity of $K_{\rm DP}$ estimates), and the self-consistency (which is commonly used to calibrate radar) are compared using simulated data. Each of these methods has weaknesses when dealing with PRD that is severely affected by measurement or model error.

To improve $K_{\rm DP}$ estimation by efficiently utilizing different information, a hybrid method of combining LSF $K_{\rm DP}$ estimation and SC property of polarimetric variables into the LP problem as stricter constraints has been developed. This hybrid method is applied on an ideal case and on a real event to demonstrate its theoretical advantage and realistic performance. The advantage of the hybrid method is that it utilizes as much information into the estimation system as possible. The results of the ideal case and the real event suggest that it performs better than the three existing methods.

A specific method to calculate lower and upper $K_{\rm DP}$ limits from Z_H and $Z_{\rm DR}$ has been adopted. With these physical constraints, $K_{\rm DP}$ values that are too small would not exist in heavy rain areas, and $K_{\rm DP}$ values that are too large would not exist in light rain areas. Since the values of Z_H and $Z_{\rm DR}$ are not entirely precise (due to radial fluctuations and problems in the attenuation correction algorithm) and the method proposed is not perfect, future work could focus on obtaining more accurate lower and upper limits.

Estimating $K_{\rm DP}$ and $\phi_{\rm DP}$ is a necessary but not sufficient part of polarimetric data quality control [43], [44]. Errors exist in polarimetric measurements mainly because of defective radar hardware, random fluctuation, clutter environment, imperfect signal processing, attenuation of hydrometeors on high frequency radar, and so on. Even if the quality of radar hardware and observing environment is ensured, and signal processing algorithms are improved, errors still exist in measured polarimetric variables (e.g., Z_H, $Z_{\rm DR}$, $\rho_{\rm hv}$, and $\Phi_{\rm DP}$). Hybrid $K_{\rm DP}$ estimation method is based on optimal estimation theory, in which information on Z_H, $Z_{\rm DR}$, and $\Phi_{\rm DP}$ is [43] utilized to optimize $\phi_{\rm DP}$ and $K_{\rm DP}$. Future work could focus on taking measurement errors into account in the optimization to further improve the estimation performance.

ACKNOWLEDGMENT

The authors would like to thank the investigators and operators of NJU C-POL and other instruments. The publisher by accepting the manuscript for publication acknowledges that the United States Government retains a non-exclusive, paid-up, irrevocable, world-wide license to publish or reproduce the published form of this manuscript, or allow others to do so, for United States Government purposes.

REFERENCES

[1] Q. Cao, M. B. Yeary, and G. Zhang, "Efficient ways to learn weather radar polarimetry," *IEEE Trans. Educ.*, vol. 55, no. 1, pp. 58–68, Feb. 2012.

[2] E. A. Brandes, G. Zhang, and J. Vivekanandan, "Experiments in rainfall estimation with a polarimetric radar in a subtropical environment," *J. Appl. Meteorol.*, vol. 41, pp. 674–685, Jun. 1, 2002.

[3] A. V. Ryzhkov, S. E. Giangrande, and T. J. Schuur, "Rainfall estimation with a polarimetric prototype of WSR-88D," *J. Appl. Meteorol.*, vol. 44, pp. 502–515, Apr. 2005.

[4] V. Bringi and V. Chandrasekar, *Polarimetric Doppler Weather Radar: Principles and Applications*. Cambridge, U.K.: Cambridge Univ. Press, 2001.

[5] H. S. Park, A. V. Ryzhkov, D. S. Zrnić, and K.-E. Kim, "The hydrometeor classification algorithm for the polarimetric WSR-88D: Description and application to an MCS," *Weather Forecast.*, vol. 24, pp. 730–748, Jun. 1, 2009.

[6] A. V. Ryzhkov and D. S. Zrnic, "Polarimetric rainfall estimation in the presence of anomalous propagation," *J. Atmos. Ocean. Technol.*, vol. 15, pp. 1320–1330, Dec. 12, 1998.

[7] A. Ryzhkov and D. Zrnic, "Beamwidth effects on the differential phase measurements of rain," *J. Atmos. Ocean. Technol.*, vol. 15, pp. 624–634, Jun. 1, 1998.

[8] A. Ryzhkov and D. Zrnić, "Assessment of rainfall measurement that uses specific differential phase," *J. Appl. Meteorol.*, vol. 35, pp. 2080–2090, Nov. 1, 1996.

[9] J. Hubbert and V. N. Bringi, "An iterative filtering technique for the analysis of copolar differential phase and dual-frequency radar measurements," *J. Atmos. Ocean. Technol.*, vol. 12, pp. 643–648, Jun. 1995.

[10] J. Hubbert, V. Chandrasekar, V. N. Bringi, and P. Meischner, "Processing and interpretation of coherent dual-polarized radar measurements," *J. Atmos. Ocean. Technol.*, vol. 10, pp. 155–164, Apr. 1993.

[11] Z. Hu and L. Liu, "Applications of wavelet analysis in differential propagation phase shift data de-noising," *Adv. Atmos. Sci.*, vol. 31, pp. 825–835, Jul. 2014.

[12] M. Schneebeli, J. Grazioli, and A. Berne, "Improved estimation of the specific differential phase shift using a compilation of Kalman filter ensembles," *IEEE Trans. Geosci. Remote Sens.*, vol. 52, no. 8, pp. 5137–5149, Aug. 2014.

[13] M. Istok *et al.*, "WSR-88D dual polarization initial operational capabilities," in *Proc. 25th Conf. IIPS Meteorol., Ocean., Hydrol.*, Phoenix, AZ, USA, 2009, p. 15.5. [Online]. Available: http://ams.confex.com/ams/pdfpapers/148927.pdf

[14] J. Vivekanandan, G. Zhang, and M. Politovich, "An assessment of droplet size and liquid water content derived from dual-wavelength radar measurements to the application of aircraft icing detection," *J. Atmos. Ocean. Technol.*, vol. 18, pp. 1787–1798, 2001.

[15] E. A. Brandes, "Dual-polarization radar fundamentals and algorithm prospects," Nat. Center Atmos. Res., Boulder, CO, USA, Rep. Next Gen. Weather Radar Program-Oper. Support Facility, WSR-88D Commerce-Defence-Transportation, 2000.

[16] J. Testud, E. Le Bouar, E. Obligis, and M. Ali-Mehenni, "The rain profiling algorithm applied to polarimetric weather radar," *J. Atmos. Ocean. Technol.*, vol. 17, pp. 332–356, Mar. 1, 2000.

[17] S. E. Giangrande, R. McGraw, and L. Lei, "An application of linear programming to polarimetric radar differential phase processing," *J. Atmos. Ocean. Technol.*, vol. 30, pp. 1716–1729, 2013.

[18] D. Bertsimas and J. N. Tsitsiklis, *Introduction to Linear Optimization*, vol. 6. Belmont, MA, USA: Athena Scientific, 1997.

[19] G. Scarchilli, E. Gorgucci, V. Chandrasekar, and A. Dobaie, "Self-consistency of polarization diversity measurement of rainfall," *IEEE Trans. Geosci. Remote Sens.*, vol. 34, no. 1, pp. 22–26, Jan. 1996.

[20] J. Vivekanandan, G. F. Zhang, S. M. Ellis, D. Rajopadhyaya, and S. K. Avery, "Radar reflectivity calibration using differential propagation phase measurement," *Radio Sci.*, vol. 38, no. 3, pp. 1–14, Mar. 12, 2003.

[21] S. E. Giangrande and A. V. Ryzhkov, "Calibration of dual-polarization radar in the presence of partial beam blockage," *J. Atmos. Ocean. Technol.*, vol. 22, pp. 1156–1166, Aug. 2005.

[22] C. D. Rodgers, *Inverse Methods for Atmospheric Sounding: Theory and Practice*, vol. 2. Singapore: World Scientific, 2000.

[23] Y. Wang and V. Chandrasekar, "Algorithm for estimation of the specific differential phase," *J. Atmos. Ocean. Technol.*, vol. 26, pp. 2565–2578, Dec. 1, 2009.

[24] R. G. Bland, "New finite pivoting rules for the simplex method," *Math. Oper. Res.*, vol. 2, pp. 103–107, 1977.

[25] W. L. Winston, M. Venkataramanan, and J. B. Goldberg, *Introduction to Mathematical Programming*, vol. 1. Belmont, CA, USA: Thomson Brooks/Cole, 2003.

[26] E. Jones, T. Oliphant, and P. Peterson, "*SciPy: Open Source Scientific Tools for Python*," 2001. [Online]. Available: http://www.scipy.org/

[27] S. E. Giangrande, S. Collis, A. K. Theisen, and A. Tokay, "Precipitation estimation from the ARM distributed radar network during the MC3E campaign," *J. Appl. Meteorol. Climatol.*, vol. 53, pp. 2130–2147, Sep. 1, 2014.

[28] M. I. Mishchenko, L. D. Travis, and D. W. Mackowski, "T-matrix computations of light scattering by nonspherical particles: A review," *J. Quantitative Spectr. Radiative Transfer*, vol. 55, pp. 535–575, May 1996.

[29] J. Vivekanandan, W. M. Adams, and V. N. Bringi, "Rigorous approach to polarimetric radar modeling of hydrometeor orientation distributions," *J. Appl. Meteorol.*, vol. 30, pp. 1053–1063, Aug. 1, 1991.

[30] J. Y. Gu *et al.*, "Polarimetric attenuation correction in heavy rain at C band," *J. Appl. Meteorol. Climatol.*, vol. 50, pp. 39–58, Jan. 2011.

[31] V. Bringi, V. Chandrasekar, N. Balakrishnan, and D. Zrnic, "An examination of propagation effects in rainfall on radar measurements at microwave frequencies," *J. Atmos. Ocean. Technol.*, vol. 7, pp. 829–840, 1990.

[32] L. D. Carey, S. A. Rutledge, D. A. Ahijevych, and T. D. Keenan, "Correcting propagation effects in C-band polarimetric radar observations of tropical convection using differential propagation phase," *J. Appl. Meteorol.*, vol. 39, pp. 1405–1433, Sep. 2000.

[33] A. V. Ryzhkov, S. E. Giangrande, V. M. Melnikov, and T. J. Schuur, "Calibration issues of dual-polarization radar measurements," *J. Atmos. Ocean. Technol.*, vol. 22, pp. 1138–1155, Aug. 1, 2005.

[34] G. Zhang, J. Vivekanandan, and E. Brandes, "A method for estimating rain rate and drop size distribution from polarimetric radar measurements," *IEEE Trans. Geosci. Remote Sens.*, vol. 39, no. 4, pp. 830–841, Apr. 2001.

[35] C. W. Ulbrich, "Natural variations in the analytical form of the raindrop size distribution," *J. Clim. Appl. Meteorol.*, vol. 22, pp. 1764–1775, 1983.

[36] J. Vivekanandan, G. Zhang, and E. Brandes, "Polarimetric radar estimators based on a constrained gamma drop size distribution model," *J. Appl. Meteorol.*, vol. 43, pp. 217–230, Feb. 1, 2004.

[37] Q. Cao, G. Zhang, E. Brandes, T. Schuur, A. Ryzhkov, and K. Ikeda, "Analysis of video disdrometer and polarimetric radar data to characterize rain microphysics in Oklahoma," *J. Appl. Meteorol. Climatol.*, vol. 47, pp. 2238–2255, Aug. 1, 2008.

[38] D. T. Dawson, E. R. Mansell, Y. Jung, L. J. Wicker, M. R. Kumjian, and M. Xue, "Low-level ZDR signatures in supercell forward flanks: The role of size sorting and melting of hail," *J. Atmos. Sci.*, vol. 71, pp. 276–299, Jan. 1, 2013.

[39] M. R. Kumjian and A. V. Ryzhkov, "The impact of size sorting on the polarimetric radar variables," *J. Atmos. Sci.*, vol. 69, pp. 2042–2060, Jun. 1, 2012.

[40] E. Gorgucci, G. Scarchilli, and V. Chandrasekar, "Specific differential phase estimation in the presence of nonuniform rainfall medium along the path," *J. Atmos. Ocean. Technol.*, vol. 16, pp. 1690–1697, Nov. 1, 1999.

[41] C. E. Shannon, "A mathematical theory of communication," *ACM SIGMOBILE Mobile Comput. Commun. Rev.*, vol. 5, pp. 3–55, 2001.

[42] S. E. Giangrande and A. V. Ryzhkov, "Estimation of rainfall based on the results of polarimetric echo classification," *J. Appl. Meteorol. Climatol.*, vol. 47, pp. 2445–2462, Sep. 1, 2008.

[43] K. Friedrich, M. Hagen, and T. Einfalt, "A quality control concept for radar reflectivity, polarimetric parameters, and Doppler velocity," *J. Atmos. Ocean. Technol.*, vol. 23, pp. 865–887, Jul. 2006.

[44] D. A. Marks, D. B. Wolff, L. D. Carey, and A. Tokay, "Quality control and calibration of the dual-polarization radar at Kwajalein, RMI," *J. Atmos. Ocean. Technol.*, vol. 28, pp. 181–196, Feb. 2011.

Hao Huang received the B.S. degree in meteorology from Nanjing University, Nanjing, China, 2011.

From 2011 to 2013, he was a Weather Forecaster with Bengbu Meteorological Bureau, Bengbu, China. In 2015, he was a Visiting Scholar with the Advanced Radar Research Center, The University of Oklahoma, Norman, OK, USA. He is currently working toward the Ph.D. degree in meteorology with the School of Atmospheric Sciences, Nanjing University. His main research interests include data processing and applications of polarimetric radar data for quantitative precipitation estimation and forecasting.

Guifu Zhang (S'97–M'98–SM'02) received the B.S. degree in physics from Anhui University, Hefei, China, in 1982; the M.S. degree in radio physics from Wuhan University, Wuhan, China, in 1985; and the Ph.D. degree in electrical engineering from the University of Washington, Seattle, WA, USA, in 1998.

From 1985 to 1993, he was an Assistant and Associate Professor with the Department of Space Physics, Wuhan University. In 1989, he worked as a Visiting Scholar with the Communication Research Laboratory in Japan. From 1993 to 1998, he studied and worked in the Department of Electrical Engineering, University of Washington, where he was first a Visiting Scientist and later a Ph.D. student. From 1998 to 2005, he was a Scientist with the National Center for Atmospheric Research. After that, he joined the School of Meteorology, University of Oklahoma, Norman, OK, USA, where he is currently a Professor. He modeled and calculated wave scattering from fractal trees and that from a target buried under a rough surface. He explored the detection of targets in the presence of clutter using angular correlation functions. He developed algorithms for retrieving raindrop size distributions. He led to develop advanced signal processing to improve weather radar data quality. He formulated theory of weather radar interferometry and that of phased array radar polarimetry. He has three U.S. patent awards, filed more than ten intellectual property disclosures, and published over 100 journal papers and the book *Weather Radar Polarimetry* (CRC Press, 2016). His research interests include wave propagation and scattering in random and complex media, remote sensing theory and technology for geophysical applications, algorithms for retrieving physical states and processes, cloud and precipitation microphysics and model parameterization, target detection and classification, clutter identification and filtering, radar signal processing, and optimal estimation. He is currently interested in the design and development of polarimetric phased array radars for weather measurements and multimission capability and weather radar polarimetry.

Kun Zhao received the B.S. degree in atmospheric physics and atmospheric environment and the Ph.D. degree in meteorology from Nanjing University, Nanjing, China, in 1998 and 2004, respectively.

Since 2004, he has been with the School of Atmospheric Sciences, Nanjing University, as an Instructor, Associate Professor, and a Professor. From 2005 to 2006, he was a Postdoctoral Researcher working at the P3 Mesoscale Meteorology Research Laboratory, National Taiwan University, Taipei, Taiwan. From 2008 to 2010, he was a Visiting Scholar with the Center for Analysis and Prediction of Storms, Oklahoma University, Norman, OK, USA. He is currently also the Director of Joint Center for Atmospheric Radar Research sponsored by the China Meteorological Administration and Nanjing University. His research interests include developing advanced remote sensing techniques, applying weather radar observations to analyze and predict severe weather.

Scott E. Giangrande received the B.S. degree in meteorology from The Pennsylvania State University, State College, PA, USA, in 2000 and the M.S. and Ph.D. degrees in atmospheric sciences from The University of Oklahoma, Norman, OK, USA, in 2002 and 2007, respectively.

From 2008 to 2010, he was a Postdoctoral Fellow with McGill University, Montreal, QC, Canada. His accomplishments include the development of novel scanning precipitation (weather) radar, cloud radar, UHF wind profiler, and multisensor techniques for rainfall and drop size distribution estimation, convective cloud vertical air motion retrievals and mass flux profiling, and hydrological (echo) classification. The activities cover a diverse range of Department of Energy (DOE) surface instrumentation and the polarimetric prototype of the NOAA-National Weather Service NEXRAD WSR-88D radar network. At the Brookhaven National Laboratory, his research interests emphasize applications for fixed and mobile facility DOE cloud and precipitation instrumentation to within challenging global deployments for the improvement of regional cloud resolving to global climate modeling capabilities. Recent activities include service as a co-investigator for the DOE-NASA Midlatitude Continental Convective Clouds Experiment (MC3E) in 2011 (Oklahoma) and again on the 2014–2015 DOE Observations and Modeling of the Green Ocean Amazon (GoAmazon2014/5) campaign.